AN ABSTRACT OF THE THESIS OF

Erin M. Moore for the degree of Master of Science in Atmospheric Sciences presented on July 25, 2002.
Title: Flow over Surface Discontinuities in a Marine Environment.

Redacted for privacy

Abstract approved: _____

Larry Mahrt

This study concentrates on analysis of LongEZ aircraft data taken offshore of the Atlantic Coast of the United States. Due to the land structure of the region, it was possible to isolate the effect of narrow land on air as it flows offshore. The narrow land (Outer Banks) separates inland water from the sea. With greater land fetch, the internal boundary layer (IBL) over land grows deeper and the eddies presumably grow larger. Larger eddies typically decay more slowly than smaller eddies, and so the turbulence advected from land with a larger land fetch should survive longer over the sea and be greater in magnitude than that with smaller land fetch. The turbulence is studied using aircraft eddy correlation data as the flow is advected over the water. As expected, greater and longer-lasting turbulence is present downstream from greater land widths.

Aircraft data taken over the Gulf Stream (GS) boundary are analyzed to study the effects of the sea surface temperature (SST) front on downstream boundary layer structure. Unstable and stable flows are studied in this region. The stable flow case is found to have an upside-down structure, with greater turbulence aloft causing stress convergence at the surface, which acts to accelerate the flow. The local thermally generated pressure gradient is important in the momentum budget across the GS front in both flow cases. A synthetic aperture radar (SAR) image is analyzed qualitatively in the region between the Atlantic Coast and the Gulf Stream front for intercomparison of data and to examine the influences of varying static stabilities and surface conditions upon the backscatter shown in satellite images.

The growth rates of the internal boundary layer due to flow over a heterogeneous surface including flow from land over the water and flow between cooler water and warmer water are calculated. These results are compared to similar calculations of growth rates from previous experiments. It is found that the growth rate of an internal boundary layer is dependent on surface roughness, despite the inclusion of σ_w in the normalization of the growth rate.

Flow over Surface Discontinuities in a Marine Environment

by
Erin M. Moore

A THESIS

submitted to

Oregon State University

in partial fulfillment of
the requirements for the
degree of

Master of Science

Presented July 25, 2002
Commencement June 2003

Master of Science thesis of Erin M. Moore presented on July 25, 2002.

Approved:

Redacted for privacy

Major Professor, representing Atmospheric Sciences

Redacted for privacy

Dean of College of Oceanic and Atmospheric Sciences

Redacted for privacy

Dean of Graduate School

I understand that my thesis will become part of the permanent collection of Oregon State University libraries. My signature below authorizes release of my thesis to any reader upon request.

Redacted for privacy

Erin M. Moore, Author

ACKNOWLEDGMENTS

I would like to thank Dr. Larry Mahrt for recruiting, advising and supporting me through my studies and research. Even when up against a deadline, Larry always has time for a laugh. I'd also like to thank him for putting up with my amazing ability to procrastinate, and for trusting me when I told him not to panic.

I would like to express my appreciation for the thousands of questions, often very dumb ones, that Dean Vickers answered for me over the years, specifically with regard to APAK programming. I could not have survived without his help.

I thank Dr. Jim Coakley for the experience of working in his lab; Jim made me realize that computer programming is actually fun! I thank him for teaching the hardest class in the program (Atmospheric Radiation) and loving it. But mostly I thank him for his support and concern for me these past few years.

I would like to thank my committee members, Drs. Vong and Higdon. Rick shows such enthusiasm for teaching and for his subject matters, it would be hard not to love atmospheric chemistry and the classes he teaches. Bob provided me with much entertainment, not to mention great instruction, during my undergraduate years in Mathematics.

I thank John Holeman and Chris Walsh for helping me through many of my classes, both in the workload and in keeping the motivation and moods

high. I could not have made it through a few classes without them.

I thank Reina Nakamura for helping me through this thesis process and always being willing to answer my questions. I also thank Craig Smith for keeping my spirits up with light conversation in the hallways, just when I thought my head might explode.

I thank my mom and dad for teaching me that anything is possible and for accepting who I am without a moment's thought. I would not be here if it weren't for your love, support, and friendship.

Last, but certainly not least, I thank my wonderful friends, Molly Monroe, Melissa Schultz, Emily Cosci (and Joshy!), Dana McGuire, Heidi Zhang, and so many others far away. Keeping the (in)sanity and hilarity in life is always much needed. Thanks for everything always.

This research was funded by the Office of Naval Research, Marine Meteorology, Grants N000149710279 and N000149810552, as well as the Oregon Space Grant Fellowship Program.

TABLE OF CONTENTS

LIST OF FIGURES

LIST OF FIGURES (CONTINUED)

LIST OF TABLES

Flow over Surface Discontinuities in a Marine Environment

1. INTRODUCTION

As air flows over a surface temperature discontinuity, an internal boundary layer is expected to develop as the air near the surface adjusts to the change in surface conditions. With offshore flow, the air advected from the land must adjust to the less rough sea surface as well as the surface temperature change. Unstable internal boundary layers, as with flow of cool air over warm water or land, have been studied in detail and have well understood growth patterns. The warmer surface warms the cooler air due to significant upward heat flux. Stable internal boundary layers, however, are far less understood and their formation is complex (Vickers et al., 2001). The stable case (e.g., warm air flowing over cooler water) does not seem to follow traditional internal boundary layer theory (Mahrt et al., 2001a).

In a stable flow case, three responses to a surface discontinuity can be hypothesized. With a small surface temperature discontinuity, a new internal boundary layer may not develop as the air above the surface simply adjusts to the new conditions without changing its structure (Mahrt, 2000). With a larger surface discontinuity, a stable internal boundary layer develops in

response to the new surface conditions and the turbulence above the stable layer, which was a part of the old boundary layer, decays downstream.

In the third case, with flow of warm air over much cooler water, a thin stable layer develops close to the surface. Above this layer, flow which was originally part of the land-based boundary layer may become partially decoupled from the surface; this can cause flow acceleration above the stable layer, and a low-level wind maximum similar to a nocturnal jet may form (Smedman et al., 1993, 1995). The shear associated with the jet can generate turbulence which occasionally bursts down to the surface, causing stress convergence and wind acceleration at the surface. Even without shear generation, the turbulence aloft, while in a state of decay, may in fact be greater than that at the surface due in part to buoyancy destruction, which can cause collapse of turbulence near the surface. This leads to an "upside-down" structure due to advection of turbulence aloft. The surface is no longer the source of turbulence; it is brought down from aloft.

This upside-down case occurs with higher bulk Richardson number (R_B). As the surface temperature difference increases, or the wind speed decreases, R_B increases and the internal boundary layer becomes more stable. With a large decrease in surface temperature, the forming stable IBL causes the upper level flow to become detached from the surface. The critical stability required for this case to occur is not known.

Traditional boundary layer theory holds that the momentum flux and corresponding surface fluxes decrease with height and approximately vanish

at the top of the boundary layer. Turbulence above the boundary layer is negligible. According to traditional boundary layer theory, the surface is the primary source of turbulence in the boundary layer. The upside-down boundary layer structure described above does not follow traditional theory as the turbulence does not decrease with height and the stress divergence may actually accelerate the flow instead of acting as a drag.

This study analyzes flow that obeys traditional boundary layer theory, as well as flows that do not. The experimental location and data set are described in Section 2. The variation in advected turbulence in offshore flow for varying upstream land fetch is studied in Section 3. Section 4 presents the Gulf Stream analyses, including estimation of the momentum budget (Sections 4.2.2 and 4.2.3) and calculation of the bulk Richardson number (Section 4.2.4) for the unstable and stable flow cases. A synthetic aperture radar (SAR) image is analyzed in Section 4.2.5 over the Gulf Stream and further west toward the coast. In Section 5, the rate of internal boundary layer growth is presented and calculated for both near-shore and Gulf Stream flights, and is compared with the growth rates calculated in previous experiments for analysis of the effects of different up- and down-stream surfaces on IBL growth. Section 6 presents conclusions.

2. THE DATA

This study analyzes data taken on and off the coast of the Outer Banks, near Duck, North Carolina. The Outer Banks is a barrier island with 2-4 story vacation homes and commercial buildings built along most of its length in the experiment region. These buildings cause large roughness lengths, which induce significant turbulence as air flows over the land, despite the narrowness of the land surface. The Outer Banks ranges from about 1 to 5 km in width in the region of the aircraft flights. It is this difference in land width that is utilized to study the terrain-influenced signatures over the water.

The Shoaling Wave Experiment (SHOWEX) took place 26 October-12 November 1997, 2-18 March 1999, and 11 November-5 December 1999. The National Oceanic and Atmospheric Administration (NOAA) LongEZ (N3R) aircraft is equipped with a Best Aircraft Turbulence (BAT) probe, which measures mean and turbulent wind parameters. These data were collected at 50 samples per second, at approximately 55 ms^{-1} airspeed, which corresponds to a sample interval of about 1 m. Flights were made parallel and perpendicular to the coast, at varying heights over the mainland, the Outer Banks, the Abermarle Sound, and the Atlantic Ocean. Slant and spiral soundings were also taken at various locations for the analysis of vertical structure of the boundary layer. Descriptions of the LongEZ's objectives and specific flight patterns in SHOWEX for the Spring and Fall of 1999 can be found in Crescenti et al. (1999) and French et al. (2000), respectively. Sun

et al. (2001) include a detailed description of instrumentation, flights, and data processing in their paper. The aircraft data were subjected to quality control procedures described in Vickers and Mahrt (1997).

The flight patterns studied in this work include repeated flight tracks parallel to the coast at varying heights above the surface and distances from shore. The lowest levels were approximately 10 m above the sea surface, the highest were about 300 m in height. Also, flights perpendicular to shore that extend about 100 km east of the North Carolinan coast are analyzed to study the various flows over the Gulf Stream, the current of warm water originating in the Gulf of Mexico and flowing northward along the East Coast of the U.S. The data taken at the lowest levels were assumed to represent surface values in this study, though it is realized that 10-m fluxes are not truly representative of those at the surface.

Data from a land tower located in Duck are also utilized. Ten thermocouples were installed at heights from about 2 m to about 35 m, with an approximate 4-m spacing between instruments. These instruments provide air temperature profiles over land, from which is inferred the structure of the unstable boundary layer in westerly flow.

Synthetic aperture radar (SAR) images taken during SHOWEX correspond with some LongEZ flights for comparisons between remotely sensed and direct measurements. The dates of SAR flights during the field program are 11, 19, 25, and 26 November and 3 and 5 December. SAR images are used to qualitatively show the difference in ocean backscatter seen by the

instrument, and how these backscatter differences can be indicative of surface stress and atmospheric stability over the ocean. The SAR image used in this study is a wide-beam RADARSAT image processed by the Canadian Space Agency and received by the Canada Centre for Remote Sensing. It is an uncalibrated image with a pixel size of 250 m, from 20 x 20 averaging of 12.5 m pixels. The SAR image is compared with advanced very high resolution radiometer (AVHRR) data from Johns Hopkins Ocean Remote Sensing Group that show the sea surface temperature (SST) in the region of the Gulf Stream front. This image has 1.25 km pixel size and is taken from AVHRR data for a time interval of 2.63 days ending 25 Nov. at 1736 (EST).

3. ALONG-SHORE SPATIAL VARIATIONS WITH OFFSHORE FLOW

The purpose of this study of offshore flow is to determine the effect that differences in land width would have on certain boundary layer characteristics. Winstead and Mourad (2000) and Winstead and Young (2000) used synthetic aperture radar (SAR) imagery to show a connection between land surface variations and terrain-induced signatures over the water in offshore flow. In this study, aircraft data are used to examine a similar connection between the width of land between inland water and the sea and the turbulence measured in the downstream flow over the sea. SHOWEX took place on the Outer Banks, a narrow strip of land between the Abermarle Sound and the Atlantic Ocean (Figure 1). Because of this land structure, analysis of the effect of a varying width of upstream land is possible, as the air has presumably lost the influence of the mainland in its travel over the Sound. When data from just downstream of the Outer Banks are analyzed, it is possible to isolate the effect of the Outer Banks.

3.1 ANALYSIS

Flights parallel to the shore are used to ensure an approximately constant sea fetch. Data are selected with wind directions of 190-310 degrees to ensure offshore flow. All data used are during days of stable flow, with flow of warmer air over cooler water. Days with less than two aircraft runs at a given height

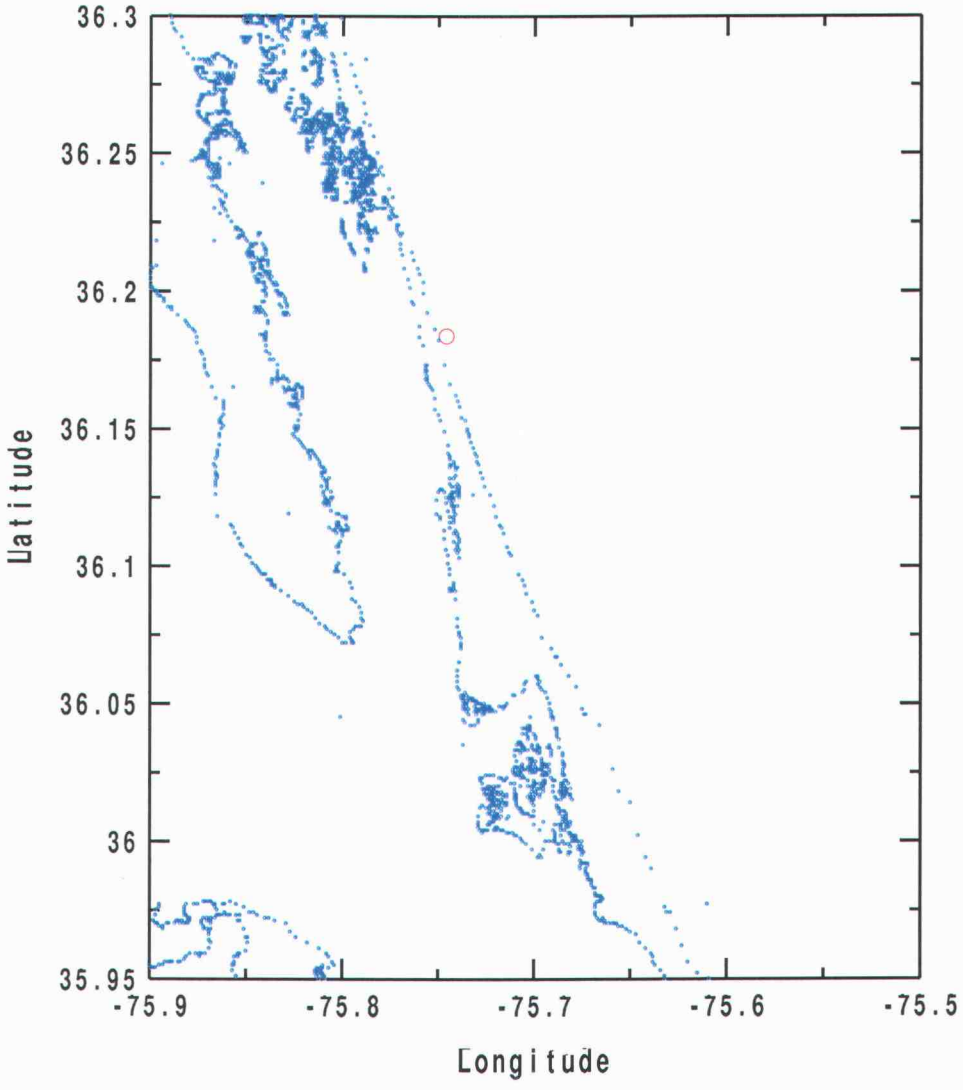

Figure 1: Map of the SHOWEX data collection site, Outer Banks, NC, USA. Red circle shows location of tower at Duck.

and distance offshore were excluded from analysis in that height-distance class. The days of stable offshore flow that met all criteria are 4, 16, and 18 March 1999, 2 and 9 November 1997, and 4 December 1999. In order to examine the influence of advection of turbulence from land on the structure of the flow and the scale of the advection over the water, the data are separated into those near the shore (less than 2 km sea fetch), mid-distance from the shore (2 km to 5 km sea fetch) and far from shore (greater than 5 km sea fetch). This estimate of the division between the near- and mid-distance cases is made by observations of the differences in behavior of the turbulence as the distance increased offshore, as will be discussed in Section 3.2. The division between the mid- and far-distance cases is arbitrary. In order to estimate the vertical structure of the flow, the data are also separated into low- and high-level flights, with the low level assigned to be less than 30 m in height. The high level is assigned to be $30m < z < 250m$, representing altitudes that are generally still within the advected land boundary layer. A very high level case is specified, when available, to be greater than 250 m in height. Turbulence for each class of data is analyzed as a function of latitude, longitude, sea fetch, and land fetch, where sea fetch is the distance over water upstream from the measurement and land fetch is the distance over land upstream. Both fetches depend on wind direction.

The friction velocity at any level is defined as

$$u_* = (\overline{w'u'}^2 + \overline{w'v'}^2)^{0.25} \tag{1}$$

and the drag coefficient is defined as

$$c_D = \frac{u_*^2}{U^2} \tag{2}$$

where primes denote fluctuations from a 1-km mean, overbars symbolize 1-km averages, and U is the wind speed computed from averaged wind components. c_D is not always a drag coefficient in the typical sense, as the levels in this study are sometimes above the surface layer, and it thus does not satisfy Monin-Obukov similarity theory. Also, in some cases, a surface layer may not be definable due to the strong influence of advection (Vickers et al., 2001). In these cases, c_D can be thought of as a normalized stress.

Plots are created using bin-averaging of 2-km unweighted, averaged scalars and fluxes in a given height and fetch class. Bin-averaging takes values in a designated range, in this case a latitude range, and averages them.

Random flux sampling errors contaminate u_* and therefore c_D. Fluxes are much more easily contaminated by random sampling errors compared to variances. For this reason, we tend to focus analysis on $\overline{w'w'}$ rather than fluxes. However, plots of c_D surprisingly show quite good correlation; using c_D partially removes the influence of variable wind speed.

3.2 RESULTS

For low observational levels, u_*, c_D, and $\overline{w'w'}$ values decrease as the sea fetch increases due to the decay of turbulence over the smoother water (Figures 2-4). Figure 3 shows the best correlation because scaling u_* by wind speed

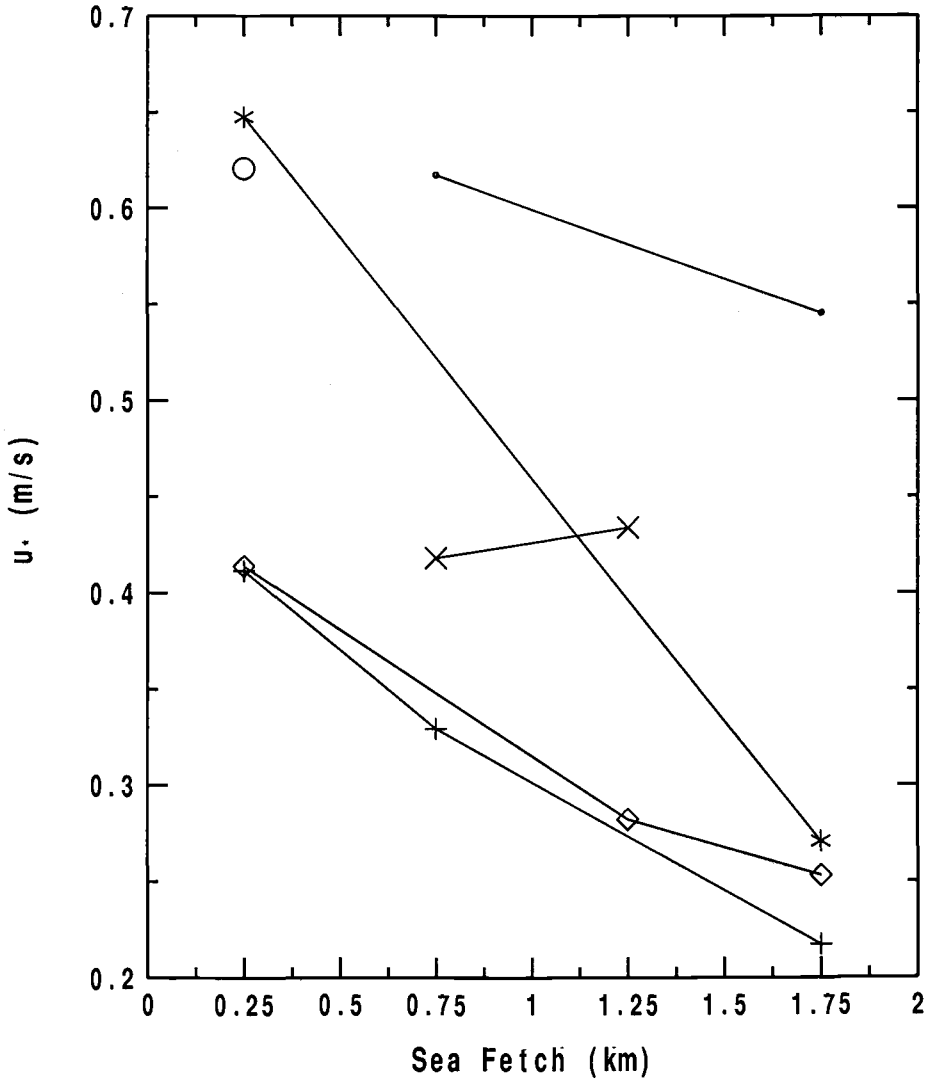

Figure 2: u_* as a function of sea fetch, $z < 30m$, sea fetch $< 2km$, for 6 study days, each day connected by a line. Flight dates with z/L values in parentheses: $\bullet$ = 03/04/99 (-0.077); $+$ = 03/16/99 (0.107); $*$ = 03/18/99 (0.289); $\circ$ = 11/02/97 (0.001); $\times$ = 11/09/97 (-0.151); $\diamond$ = 12/04/99 (0.053).

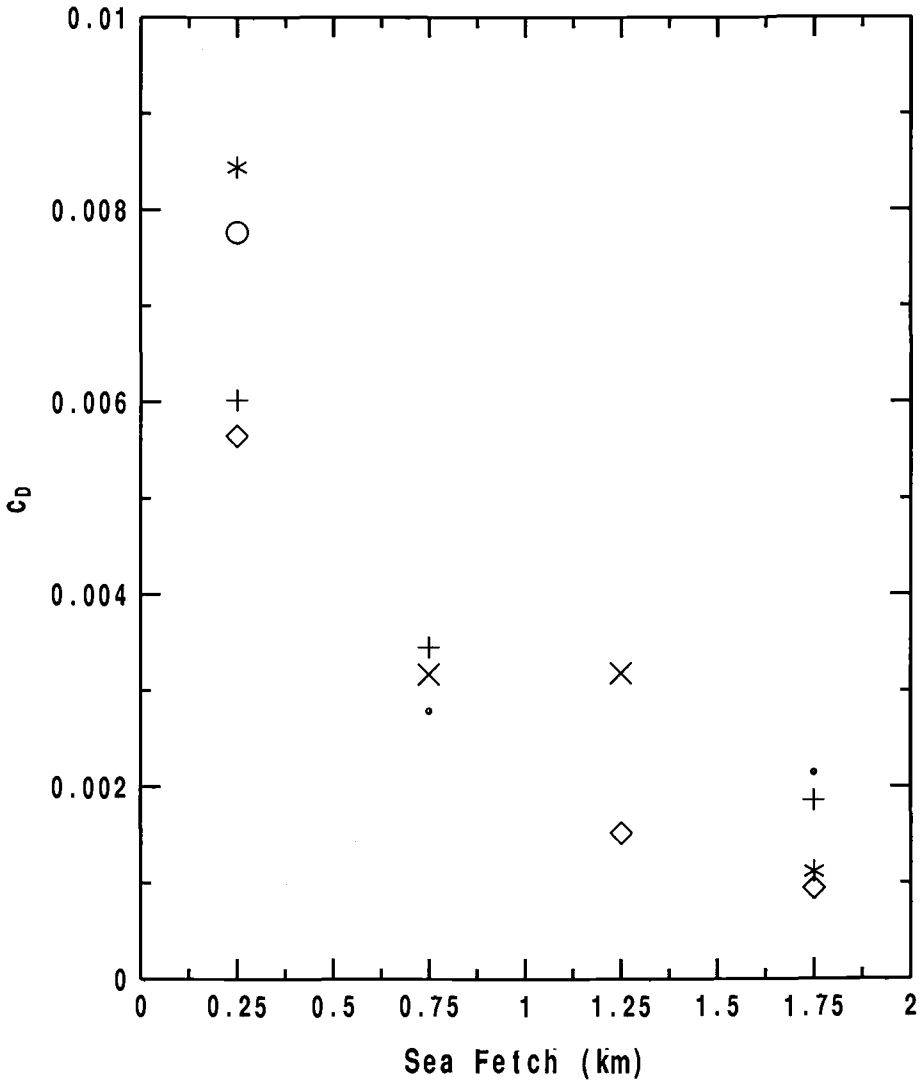

Figure 3: c_D as a function of sea fetch, $z < 30m$, sea fetch $< 2km$, for 6 study days. Flight dates with z/L values in parentheses: $\bullet$ = 03/04/99 (-0.077); $+$ = 03/16/99 (0.107); $*$ = 03/18/99 (0.289); $\circ$ = 11/02/97 (0.001); $\times$ = 11/09/97 (-0.151); $\diamond$ = 12/04/99 (0.053).

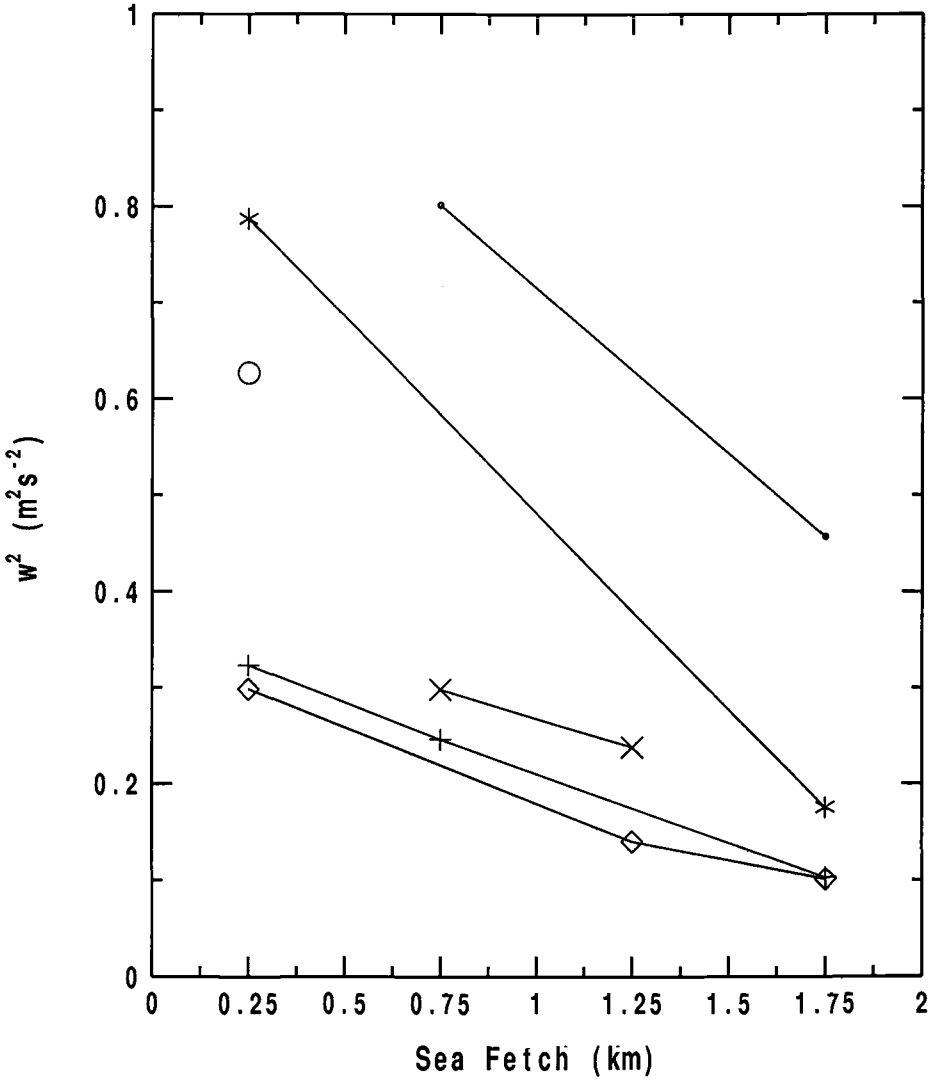

Figure 4: $\overline{w'w'}$ as a function of sea fetch, $z < 30m$, sea fetch $< 2km$, for 6 study days, each day connected by a line. Flight dates with z/L values in parentheses: $\bullet$ = 03/04/99 (-0.077); $+$ = 03/16/99 (0.107); $*$ = 03/18/99 (0.289); $\circ$ = 11/02/97 (0.001); $\times$ = 11/09/97 (-0.151); $\diamond$ = 12/04/99 (0.053).

gives a nondimensional value of the friction velocity that is not dependent on wind speed. The decay of turbulence with sea fetch is also obvious at higher levels within the boundary layer (Figure 5). Sun et al. (2001) find similar behavior of the decay of turbulence offshore using the same dataset, with runs that were perpendicular to shore included. As the turbulent air from the land is advected over the cooler water, buoyancy no longer generates turbulence but instead destroys it. Thus, the turbulence rapidly decays, adjusting to a new stable marine boundary layer.

Because the flight tracks are not perfectly parallel to the coast (as seen in Figure 6), the sea fetch of the air along the flight track varies. This variation is particularly important for flight tracks close to the coast. The relative differences in sea fetch in the close-to-shore runs (sea fetch $< 2km$) are quite large and thus are not suitable for our analyses. Hence, this study focused more on the larger distances exceeding 2 km of sea fetch.

Figure 6 shows the variation of $\overline{w'w'}$ with land fetch and sea fetch for the low-level flights. Runs with similar sea fetch are composited. The wind vectors shown are averages, thus there may be considerable wind variability between runs as well as between the three distances offshore. The variation with land fetch is strong close to shore, though the sea fetch varies for these cases, and gradually fades with distance from shore. The vertical velocity variance and boundary layer depth increase with land fetch; the more time the air spends over land (larger land fetch) and/or the slower the flow, the longer the time period for generation of turbulence. Once the air reaches the

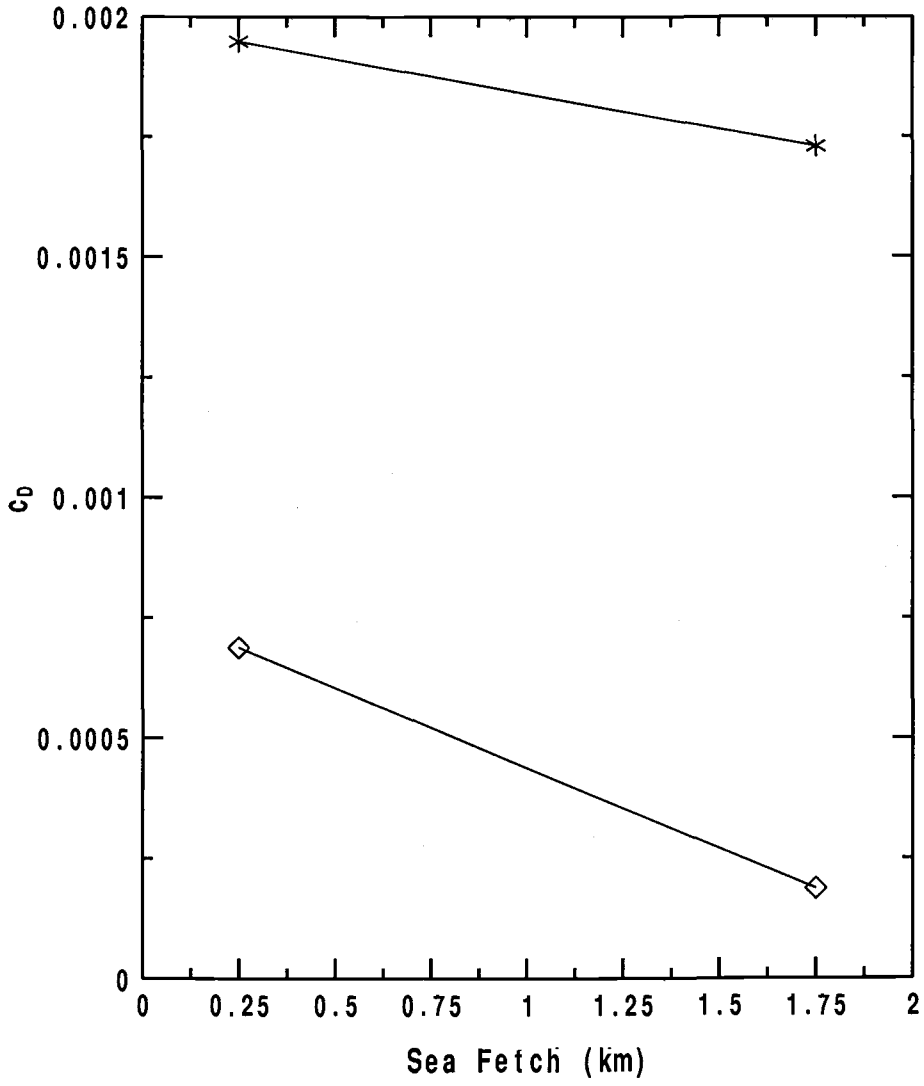

Figure 5: c_D as function of sea fetch, $30m < z < 250m$, sea fetch $< 2km$, for 2 study days, each day connected by a line. Flight dates with z/L values in parentheses: $*$ = 03/18/99 (0.158); $\diamond$ = 12/04/99 (4.099).

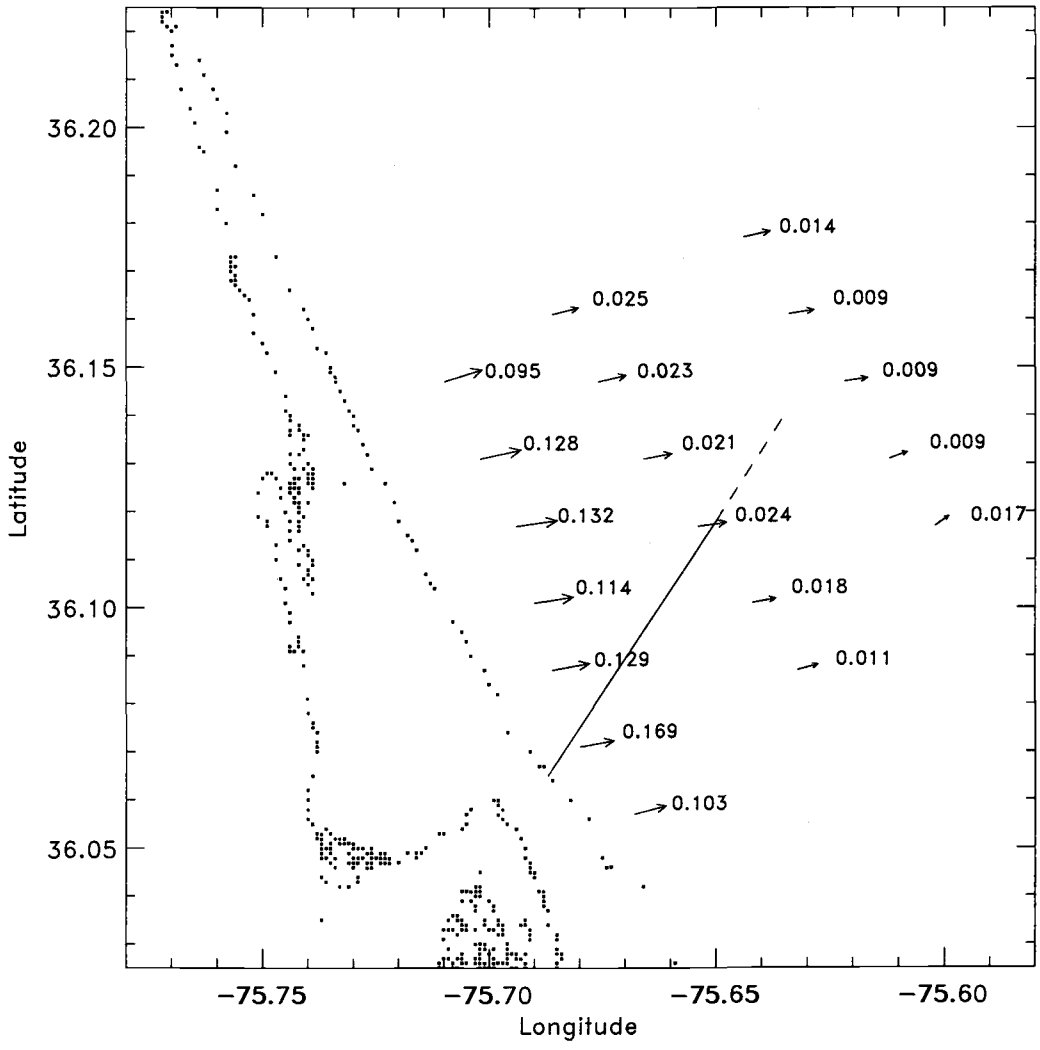

Figure 6: $\overline{w'w'}$ plotted on a map of the Outer Banks, $z < 30m$. Wind vectors are shown. Line shows an estimate of the movement of the maximum vertical velocity variance.

water, the turbulence decays rapidly due to downward heat flux and smaller surface roughness over the sea. This decay is obvious in the plots, as $\overline{w'w'}$ decreases with increasing distance offshore.

One can see that the maximum $\overline{w'w'}$ just offshore occurs downstream from the largest land fetch. This maximum is displaced northward farther from shore. The land footprint that the flux represents is determined by some angle of horizontal spread in the horizontal plane on the order of 45 degrees (Figure 7); the farther the measurement is from the shore, the flux will represent more of a north-south land swath. That is, horizontal mixing by the larger turbulent eddies and possible mesoscale motions diffuse information in the along-shore (north-south) direction. As the distance from shore increases, the measurement includes more length of the coastline, and so the region of the measurement that includes the largest averaged land fetches will correspond to the greatest turbulence. The more southerly values of the aircraft-measured turbulence begin to include more of the narrower southerly land region in the footprint, causing the maximum flux to be farther north farther offshore as shown by the dashed line in Figure 6. The footprint spatially integrates the land influence so as to not show sharp minimums and maximums. For example, at latitude 36.05°N, the land changes from very wide to quite narrow suddenly, but the influence of the along-shore variations is smoothed by horizontal mixing as the air flows offshore.

Fluxes from higher level flights also show a strong correlation between the magnitude of the flux and land width (Figure 8). At higher levels, the

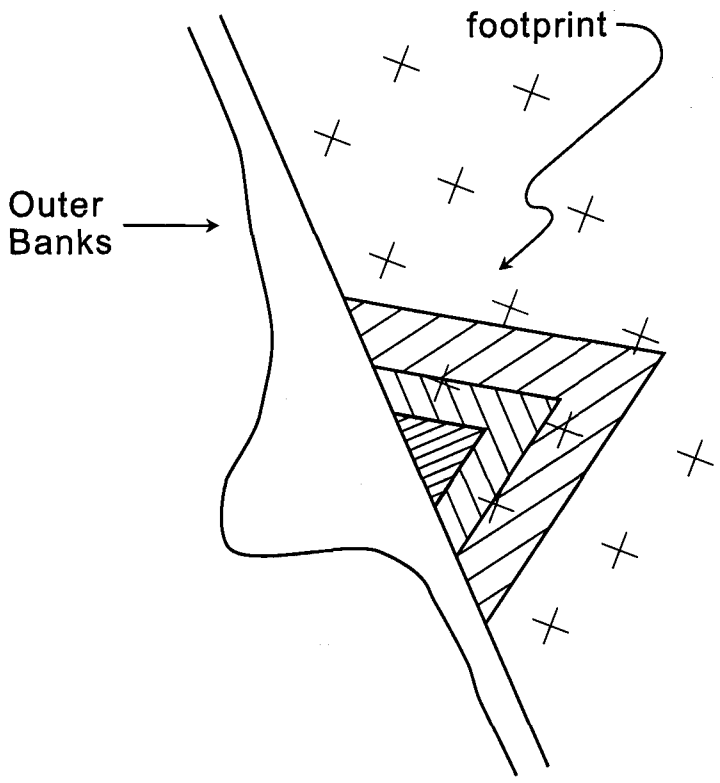

Figure 7: Schematic of the land footprint captured in the flux measurements for different distances offshore.

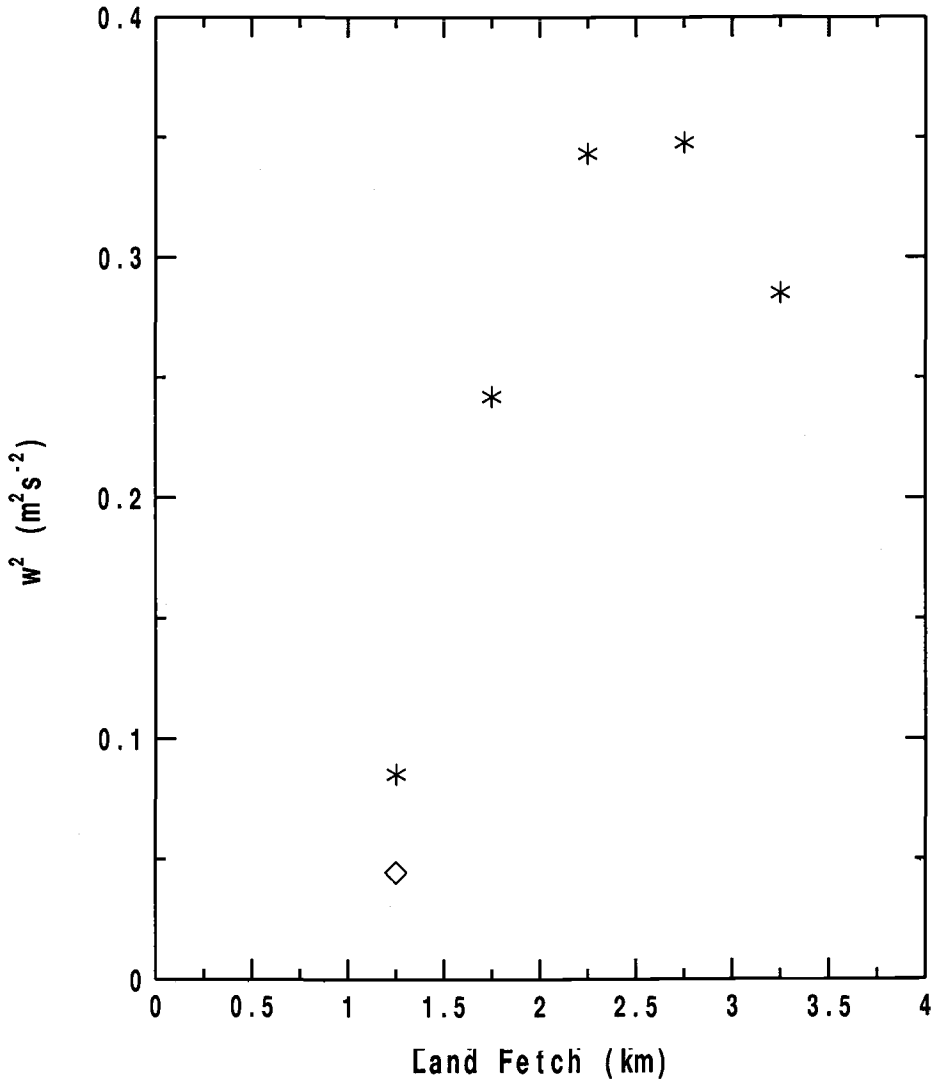

Figure 8: $\overline{w'w'}$ as a function of land fetch, $30m < z < 250m$, sea fetch $< 2km$, for 2 study days. Flight dates with z/L values in parentheses: $*$ = 03/18/99 (0.158); $\diamond$ = 12/04/99 (4.099).

footprint extends farther upstream, including more land and less of the underlying water surface. Horst and Weil (1994) suggest that the upstream footprint can be found an upwind distance of 100 times the measurement height; the required fetch for capturing a flux measurement increases for greater stability and weaker wind speed. This suggests that, for the low level (10-30 m), the upstream footprint is approximately 1-3 km upstream. For the higher level (30-250 m), the footprint can reach from 3 km to 25 km upstream. As the upstream land ranges from 1-7 km upwind from the aircraft flights that have less than 2 km of sea fetch, it can be expected that the flux measurements below about 70 m in height have footprints which extend over the upstream land. Above this height, inclusion of flux values originating from Abermarle Sound becomes probable.

In our analysis of the possible fetch for separation of near-shore from farther from shore cases, we found that beyond about 2 km fetch, the flux values were noticeably decreased from those nearer shore at the low level. Horst and Weil (1994), as explained above, predict a 1-3 km upstream footprint for a flux measurement taken below 30 m in height, depending on stability and wind speed. This prediction for the upstream footprint fits with our finding of decreased turbulence, which presumably originates from a footprint including the underlying water surface, at about 2 km sea fetch at the low level. At the very high-level ($z > 250m$), the flux dependence on land fetch breaks down (not shown). The vertical velocity variance is an order of magnitude weaker above 250 m than in the levels below. In these cases, the

measurements were probably taken above the upstream convective boundary layer and so the fluxes at this height have no origin from land. Also, Horst and Weil (1994) would predict the footprint to lie at least 25 km upstream, far beyond the Outer Banks.

Typically in stable offshore flow, the momentum flux increases with height close to the shore, partially due to the larger land footprint aloft causing high-level advection. As in Vickers et al. (2001), we find that just offshore, the momentum flux decreases with height, but farther than about 1.5 km offshore, the advected turbulence becomes partially detached from the surface, causing a momentum flux maximum aloft. This elevated maximum contrasts with traditional boundary layer theory in which the momentum flux typically decreases with height. Vickers et al. (2001) describe a combination of several factors as the cause of the elevated maximum, including stronger winds aloft causing shorter travel times for the same fetch, and downward heat flux causing greater buoyancy destruction at low levels. Smedman et al. (1993, 1995) propose that marine low-level jets form in many offshore flow cases due to frictional decoupling from the surface, which is caused in part by buoyancy destruction at surface levels. This momentum flux maximum aloft brings stronger momentum down to the surface, increasing low-level wind speed.

The far cases, of which only low-level data exist, show the same but weaker correlation between flux magnitude and land width, potentially because the footprints include mostly upstream water. In Figure 9, the days are very distinct while still generally showing an increase in flux magnitude, though

small, with increasing land fetch; the more stable cases show much smaller fluxes, as would be expected. Vickers et al. (2001) find that the momentum flux rapidly decreases with distance offshore and reaches a constant value after 6-10 km of fetch on SHOWEX offshore flow days.

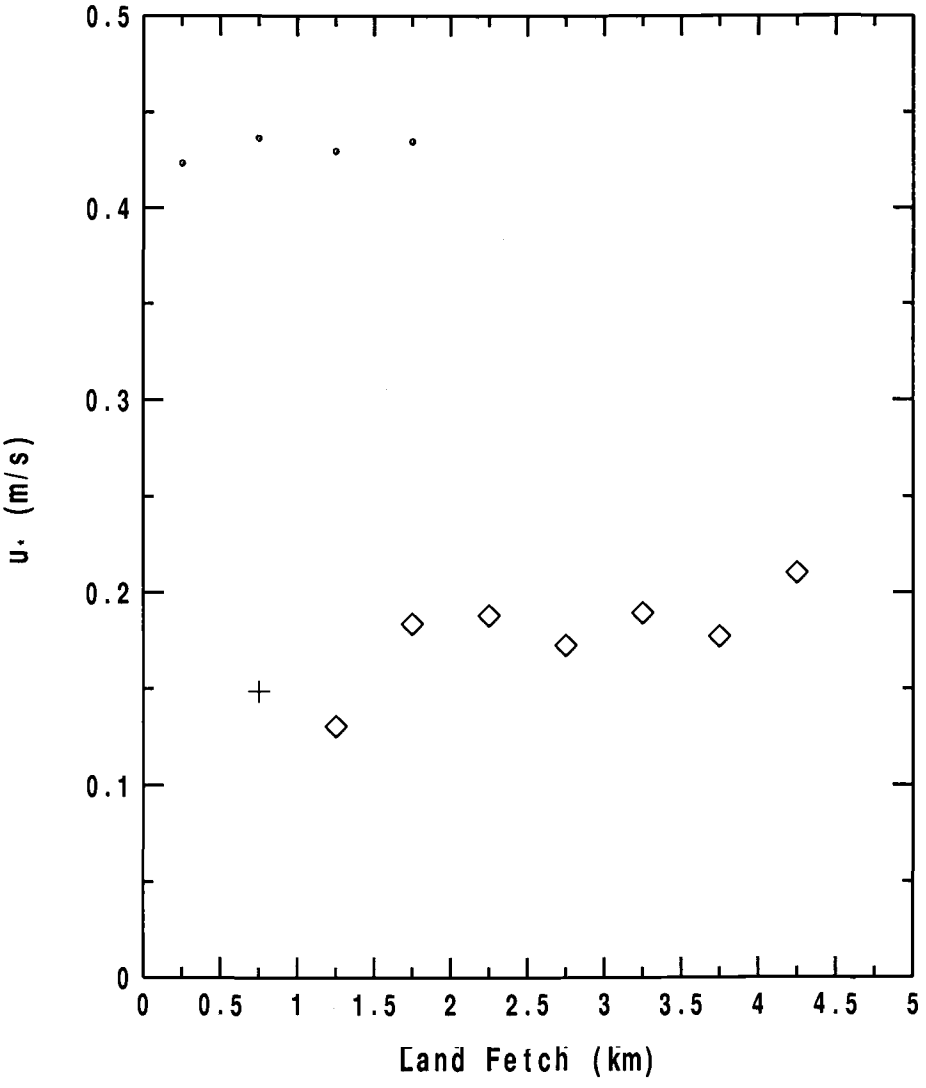

Figure 9: u_* as a function of land fetch, $z < 30m$, sea fetch $> 5km$, for 3 study days. Flight dates with z/L values in parentheses: $\bullet$ = 03/04/99 (-0.086); $+$ = 03/16/99 (0.341); $\diamond$ = 12/04/99 (0.088).

4. STUDY OF THE GULF STREAM

The Gulf Stream (GS) boundary begins approximately 90-100 km offshore of Duck, NC and flows more or less parallel (approximately SSW-NNE) to the coast. The sea surface temperature (SST) difference across the frontal boundary is typically 5-7 °C over a varying frontal zone width of 3-15 km. In this study, observation of the horizontal variation of atmospheric flow across the front using aircraft passes perpendicular to the GS front is supplemented with instantaneous observations of vertical structure through slant and spiral soundings routinely taken by the aircraft. A SAR image that coincides with a LongEZ flight that does not extend into the Gulf Stream is analyzed to compare remotely sensed and directly measured data and study the effect a SST front has on the surface stress as seen from a satellite.

4.1 ANALYSIS

LongEZ flights were taken over the Gulf Stream on 19, 20, and 22 November. On these days, the Gulf Stream frontal boundary was intersected by the aircraft between about 35 and 95 km offshore, the range due to the differing latitudes of flights and the general SSW-NNE positioning of the front. The boundary is identified by a substantial change in surface temperature. The frontal region, where the surface temperature varies rapidly with horizontal distance, is not included in the eddy correlation analyses due to ambiguity of fluxes computed from rapidly varying mean flow. Instead, we compare the

characteristics of the boundary layer between the cold and warm sides of the frontal zone. Plots are examined in terms of $\overline{w'w'}$, u_*, $\overline{w'\theta'}$, wind speed, wind direction, surface temperature, air potential temperature, and direction of the stress vector as a function of distance offshore for each valid run of each day. Potential temperature (θ) is calculated using the sea surface as $z = 0$, instead of the 1000-mb surface. In order to study spatial variation, fluxes are averaged only over a 1-km window so random flux errors are probably large. The runs with the same altitude on the same day are composited to reduce random errors; they are interpolated onto the track corresponding to the shortest run.

Over the cold water, on the west side of the GS front, fluxes are very small. Measurements taken over the warm water, on the east side of the front, show enhanced turbulence, which mixes stronger momentum downward toward the surface. The changes in turbulence across the front can be attributed to variations in buoyancy production of turbulence. The turbulence influences the sea surface roughness through downward momentum transport, which induces additional surface heterogeneity.

The three days of Gulf Stream flights were each characterized by different wind direction, corresponding to three different physical regimes. On 19 November northeasterly flow is approximately parallel to the Gulf Stream edge. 20 November is a day of unstable westerly flow. 22 November corresponds to very strong stability over the cold water due to easterly flow, from warm water over cooler water. Limited assessment of vertical struc-

ture is available for these days, with 10-m and 33-m level flights taken on 20 Nov. and 9-m, 90-m, and 280-m level flights taken on 22 Nov.; 19 Nov. includes only flights at the 9-m level. Slant and spiral soundings were, unfortunately, not taken over the warmer water east of the Gulf Stream boundary, but soundings are analyzed from over the cool water to estimate the local boundary layer structure.

4.1.1 The momentum budget

The horizontal momentum equation is

$$\frac{\partial u}{\partial t} + \vec{v} \cdot \nabla u = fv - \alpha \frac{\partial p}{\partial x} - \frac{\partial \overline{w'u'}}{\partial z} \tag{3}$$

where $\frac{\partial \overline{w'u'}}{\partial z}$ is the stress divergence between two flight levels and $\alpha \partial p/\partial x$ is due to synoptic scale pressure variations and local hydrostatic pressure gradients related to $\partial T/\partial x$. The following derivation of the thermal wind contribution to the pressure gradient force is done in z-coordinates instead of p-coordinates because the LongEZ flies at a constant height above the surface. We estimate the importance of the local hydrostatic thermal contribution using the hypsometric equation

$$p_{sfc} = p(z_T) exp(\int_0^{z_T} \frac{g}{RT} dz), \tag{4}$$

where z_T is the height of the top of the boundary layer. Temperature will be decomposed as $T = T_0 + T^*$ where T_0 is the synoptic temperature, and T^* is the local temperature perturbation induced by sea surface temperature

variations. As a rough approximation, we assume that T_0 is independent of height since we are examining shallow flows. The decay with height of the temperature perturbation due to the surface heterogeneity is expressed as

$$T^*(x,z) = f(x)exp(\frac{-z}{H_b}) \tag{5}$$

where H_b is the $1/e$ folding depth for temperature. As an example, we represent the horizontal variation of air temperature $f(x)$ in the frontal zone as a linear function, ax, where $a = \delta T_{sfc}/\delta x$, δx is the distance between constant SST on the cool side and constant SST on the warm side of the GS boundary, and δT_{sfc} is the total sea surface temperature change. After substituting Eq. 5 into Eq. 4 and rearranging, then taking the derivative with respect to x, we find that

$$\frac{\partial p_{sfc}}{\partial x} = [\frac{p(z_T)cH_ba}{HT_0} + \frac{\partial p(z_T)}{\partial x}]exp(\frac{z_T}{H} + \frac{cH_bax}{HT_0}) \tag{6}$$

where $H = RT_0/g$, the scale height of the atmosphere, $c = exp(-z_T/H_b) - 1$, and α is the specific volume of the air. Note that ax is the total horizontal change of temperature. The term $\frac{\partial p(z_T)}{\partial x}exp(\frac{z_T}{H} + \frac{cH_bax}{HT_0})$ is an interaction between the pressure gradient at z_T and the horizontal temperature gradient below, a, and is a consequence of posing the problem in z-coordinates.

The common term, $exp(\frac{z_T}{H} + \frac{cH_bax}{HT_0})$, can be approximated as 1. As an extreme example, assume a very large temperature gradient and extremely unstable conditions, as in the city heat island effect. In this case, $\frac{z_T}{H}$ may be as large as 0.25, and $\frac{cH_bax}{HT_0}$ as large as -4×10^{-3}, making $exp(\frac{z_T}{H} + \frac{cH_bax}{HT_0})$

approximately 1.3. Since these conditions are rarely met, especially over the ocean, this term can be assumed to be very near 1 for our analysis.

The term $\frac{\partial p(z_T)}{\partial x}$ is identified with the large-scale geostrophic wind and is independent of the horizontal temperature gradient; we equate this term with $fv(z_T)$ as an estimate of the synoptic pressure gradient force at the boundary layer top. The contribution of the horizontal temperature gradient to the surface pressure gradient can thus be written as

$$\frac{\partial p^*}{\partial x} = \frac{p(z_T) c H_b a}{H T_0}. \tag{7}$$

The thermal contribution to the pressure gradient as well as other terms in Eq. 3 will be evaluated in subsequent sections for the Gulf Stream frontal zone.

Due in part to data limitations, the stress divergence term is calculated between the two lower levels for multi-level flights, while the thermal contribution to the pressure gradient, the advection term, and the Coriolis term are estimated from data found at the low level. This strategy assumes that the stress divergence is linear with height and is the same at the low-level as it is between the levels. While this assumption is not valid in most cases, especially in stable conditions, we use it in order to calculate an order of magnitude estimate for the stress divergence. We assume the flow at the top of the boundary layer is the same order of magnitude as the geostrophic wind to estimate the synoptic pressure gradient force, $fv(z_T)$. The advection, Coriolis, and local pressure gradient force terms are evaluated across

the transition zone, while the synoptic pressure gradient term is evaluated on the cold, west side of the front. The vertical profiles were only flown on the cold side of the GS front, and so high level data, where we estimate the geostrophic wind, are only available there. We assume the wind does not change significantly at the top of the boundary layer across the front. The stress divergence term is estimated on either side of the GS boundary for comparison, since there is too little sampling in the transition zone for calculation of the stress divergence there. All values presented in the momentum budgets are only accurate to their order of magnitude.

4.1.2 Predictability of the Richardson number

We examine the ability of the predictive Richardson number to estimate the response of the flow downstream from a spatial change in surface temperature. The predictive Richardson number is defined as

$$R_P = \frac{g}{\overline{\theta}_{up}}(\theta_{air,up} - T_{sfc,dn})\frac{z}{U_{up}^2} \tag{8}$$

where g is the acceleration due to gravity, $\overline{\theta}_{up}$ is the mean potential temperature upstream of the surface discontinuity, $\theta_{air,up}$ is the potential temperature of the air in the upstream direction, $T_{sfc,dn}$ is the sea surface temperature downstream, and U_{up} is the wind vector magnitude on the upstream side of the boundary at height z. Eq. 8 uses the wind speed and air temperature values of the air on the upstream side of the surface discontinuity and the downstream surface temperature to predict the bulk Richardson number of

the air downstream. If successful, such a parameter would not only help categorize the response of the boundary-layer flow to surface temperature changes, but also may be of some extrapolation value. For example, in the case of offshore flow, the predictive Richardson number can be evaluated in terms of the sea surface temperature and easily measured air temperature and wind over land. Since the former is slowly changing, routine observations are not needed.

The boundary-layer response downstream from a change in surface temperature can be roughly classified into three responses. In the adjusting boundary layer (Mahrt, 2000), the surface temperature change is not sufficiently strong to alter the basic integrity of the boundary layer even though it adjusts in terms of the strength of turbulence energy and boundary-layer depth. With larger changes of surface temperature (larger predictive Richardson number), a new internal boundary layer develops in response to the new surface conditions while turbulence in the old boundary layer at higher levels decays in the downstream direction. The third possibility corresponds to flow of warm air over a much colder surface (large positive predictive Richardson number) in which case the turbulence near the surface collapses downstream from the surface temperature change where a strong surface inversion layer forms (Smedman et al., 1993, 1995). In this case, turbulence advected downstream above the surface inversion layer may be

stronger than that at the surface, even if in a state of decay. With this upside-down structure, turbulence may occasionally burst downward toward the surface.

The classical bulk Richardson number is used for comparison with the predictive Richardson number (Eq. 8):

$$R_B = \frac{g}{\overline{\theta}_{dn}}(\theta_{air,dn} - T_{sfc,dn})\frac{z}{U_{dn}{}^2} \tag{9}$$

where subscripts "dn" have been substituted for subscripts "up" to show that Eq. 9 uses the same variables as Eq. 8, but all measured downstream from the boundary in order to calculate the "true" bulk Richardson number. The predictive Richardson number assumes that the wind speed and air temperature change much more slowly than the surface temperature from one side of the surface temperature front to the other. The Richardson numbers can be used to estimate the probability of an internal boundary layer forming.

4.2 RESULTS

4.2.1 Flow parallel to the Gulf Stream boundary, 19 November

On 19 November, only 9-m height flights are available for analysis. The SST differs by about 5.7 °C over about 2.5 km and the flow is NE, parallel to the GS front. Table 1 shows fluxes, air potential temperature, and SST on either side of the GS. u_*, σ_w, and $|\overline{w'\theta'}|$ are 25%, 50%, and 190% greater, respectively, on the warm, east side of the GS than on the cold side, though the

very small fluxes on the cold side of the Gulf Stream are subject to significant sampling and instrumental errors, causing percentage increase estimates to be unreliable.

Table 1. 9-m level composites of 1-km means, 19 November.

	cold water	warm water
SST ($°C$)	19.71	25.41
$\theta(°C)$	17.74	18.85
$\overline{w'w'}$ (m^2/s^2)	0.043	0.099
u_* (m/s)	0.144	0.179
$\overline{w'\theta'}(m°Cs^{-1})$	0.012	0.035

The absolute change of these fluxes is relatively small compared to those on 20 and 22 Nov. because some upward heat flux occurs on the west, cool side of the boundary, in contrast to the other two days (Figure 10C). The wind undergoes very little change both in direction and in magnitude across the frontal boundary (Figure 11). The stress vectors in general oppose the wind and increase in magnitude slightly toward the warm side of the GS. The air-sea temperature difference is much greater on the warm side of the front (-2 °C on the cold side and -6.5 °C on the warm side). A quasi-mixed layer is present on the cool side at heights up to about 100 m on this day, as seen in the vertical profiles from a slant sounding in Figure 12.

Khalsa and Greenhut (1989) studied a SST front southwest of Bermuda with a much smaller temperature gradient, and specifically studied a day during which the flow was parallel to the front. As in this study, no change

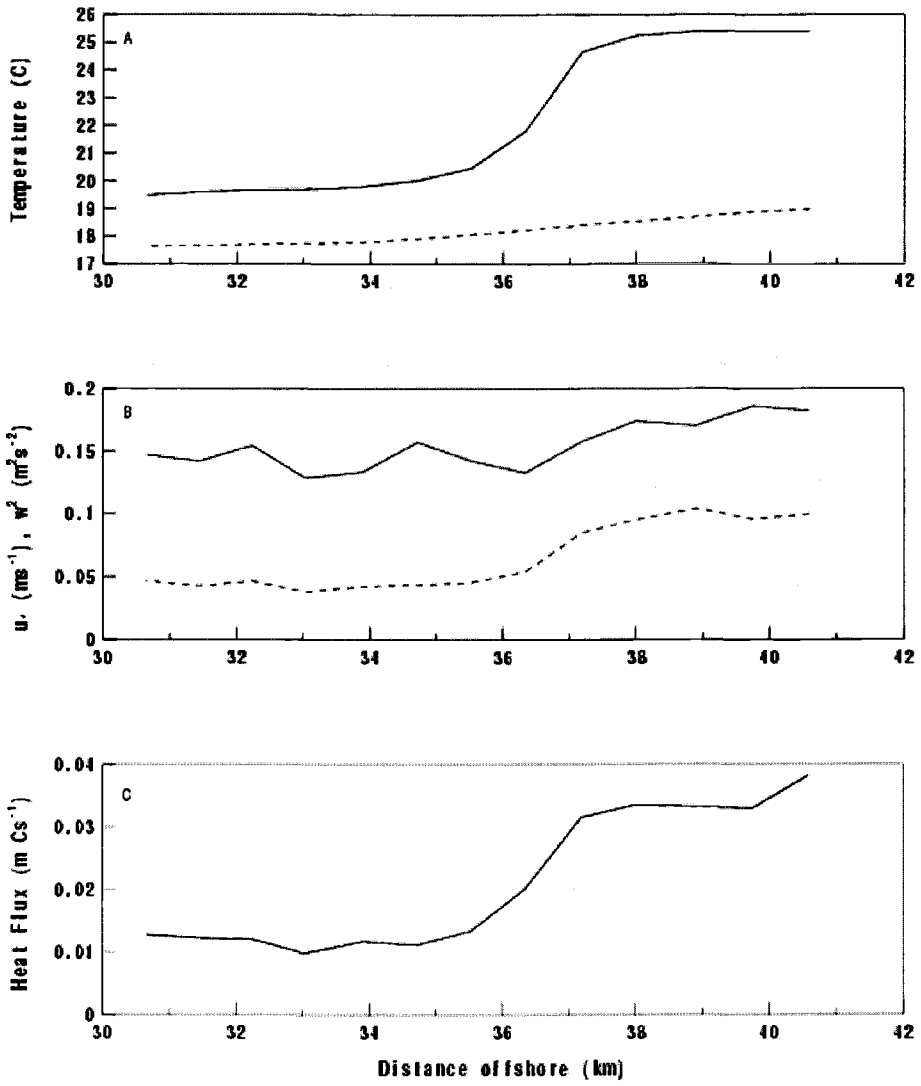

Figure 10: Composites for 19 November, 9-m height, for flow parallel to the GS front. A) Solid line is SST, dashed line is air potential temperature. B) Solid line is u_*, dashed line is $\overline{w'w'}$.

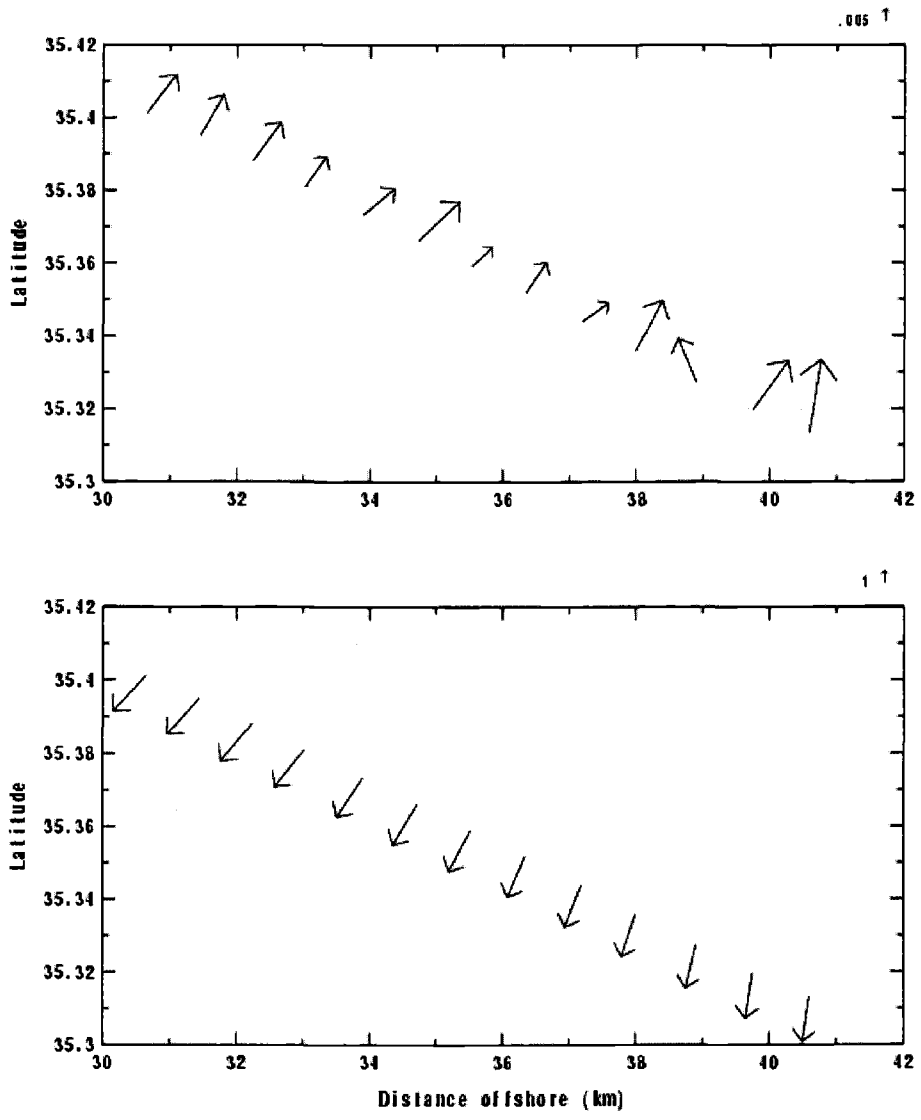

Figure 11: Composites for 19 November, 9-m height. Top plot shows stress vectors (legend shows size of 0.005 $m^2 s^{-2}$ vector), bottom plot shows wind vectors (legend shows size of 1 ms^{-1} vector).

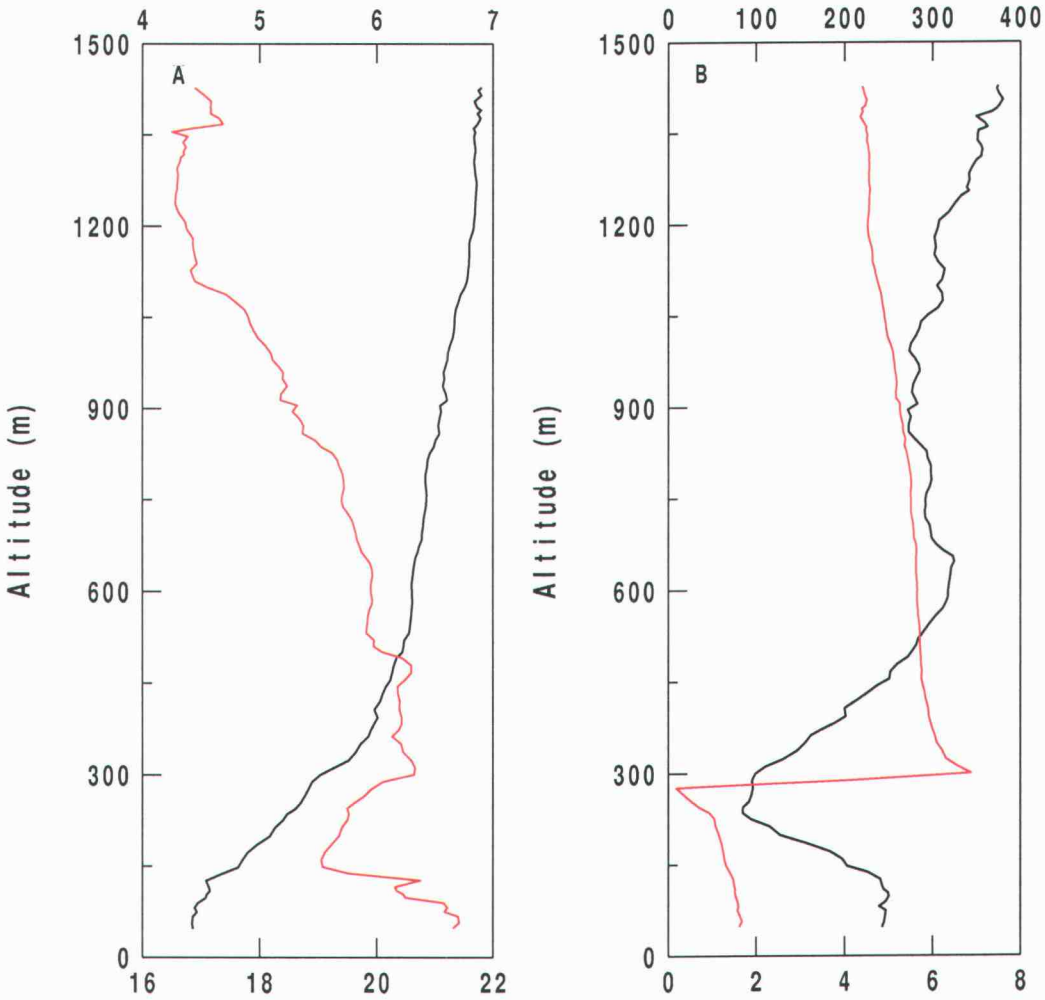

Figure 12: Vertical profile from a slant sounding on 19 Nov. A) black line is θ(°C), red line is specific humidity (gkg^{-1}). B) black line is wind speed (ms^{-1}), red line is wind direction.

in wind speed is seen across the front and the heat flux is seen to increase considerably across the boundary on the warm side. In their study, however, the momentum flux is seen to decrease on the warm side. The larger air-sea temperature difference is expected to produce more instability on the warm side and thus larger turbulent fluxes; the result they found contradicts this expectation. Our data showed the expected greater momentum flux on the warm side where the instability is greater.

4.2.2 Unstable flow over the Gulf Stream, 20 November

4.2.2.1 Spatial variation over the Gulf Stream

On 20 November, turbulence is much weaker at the 33-m level than at the 8-m level on the cool west side of the GS boundary (Figures 13 and 14), suggesting a shallow stable boundary layer on the cool side. u_* and σ_w each increase by a factor of 3 (12) across the front at the 8-m (33-m) level. The 33-m level shows a much greater increase in turbulence over the warm water than the 8-m level. The heat flux is downward but near zero at both levels on the cool side of the front, again suggesting a stable layer here, and reaches close to $+0.03\ m°Cs^{-1}$ on the warm side (Table 2). The flux values, especially on the cool side of the GS, are very small in magnitude, which causes the estimated increases across the GS front to be unreliable. The

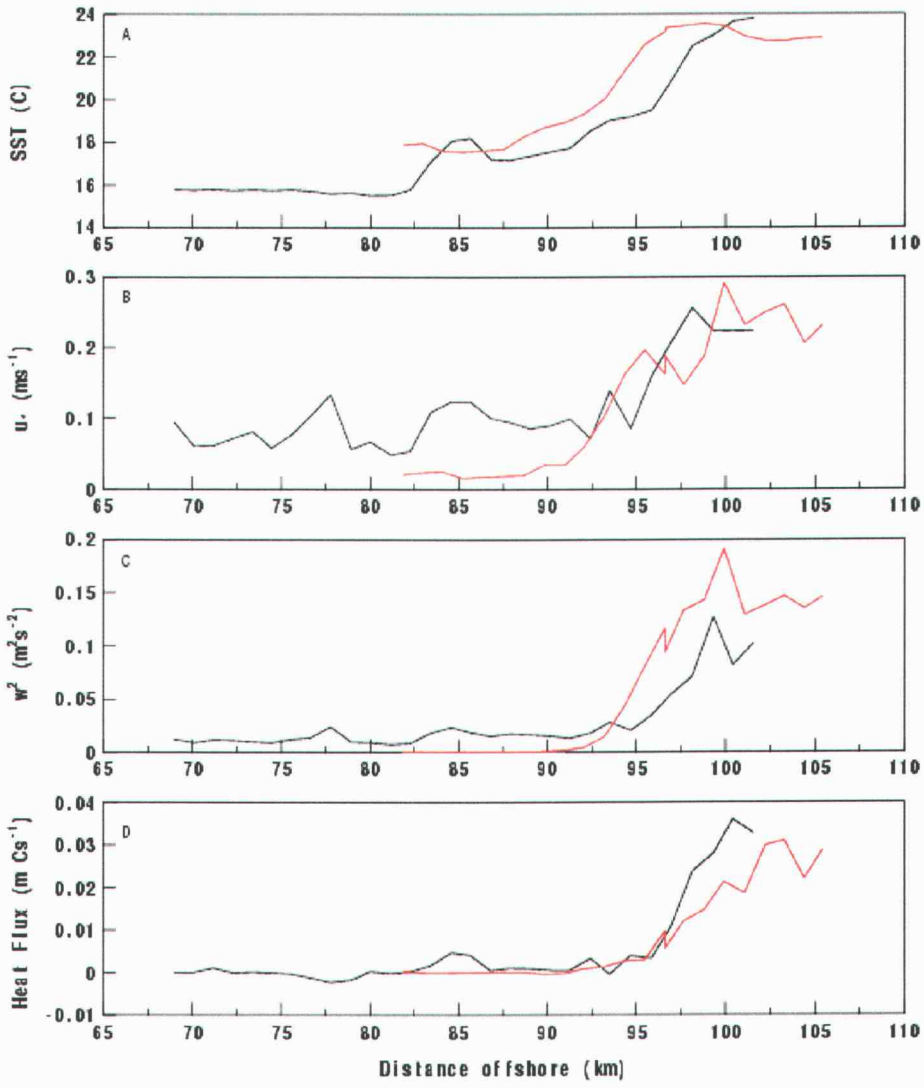

Figure 13: Composites for 20 November, 8-m (black) and 33-m (red) heights, for unstable westerly flow.

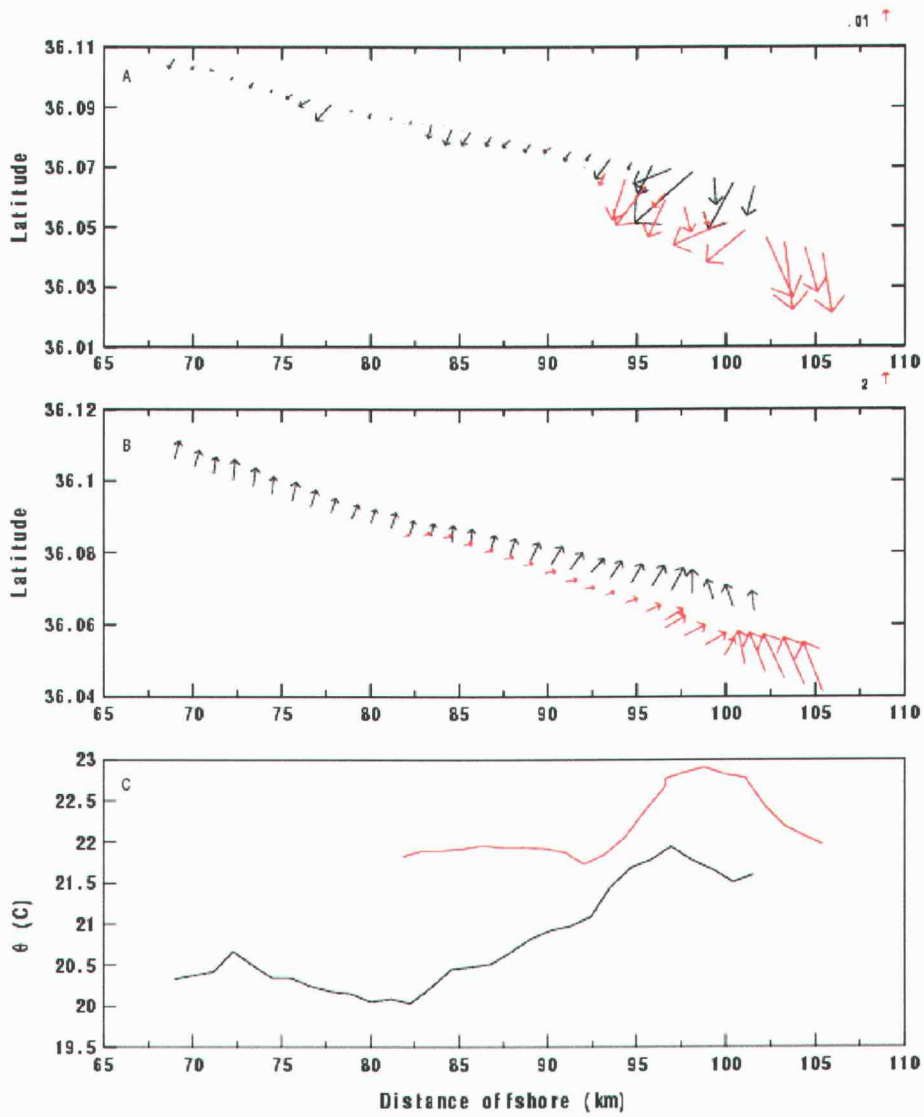

Figure 14: Composites for 20 November, 8-m (black) and 33-m (red) heights. A) stress vectors (legend shows size of 0.01 $m^2 s^{-2}$ vector), B) wind vectors (legend shows size of 2 ms^{-1} vector).

differences between fluxes over the warm and cold sides of the GS front are too small to distinguish from sampling errors in many cases.

Table 2. 8-m and 33-m level composites of 1-km means, 20 November.

	8-m level		*33-m level*	
	cold water	warm water	cold water	warm water
SST ($°C$)	15.69	23.73	17.71	23.07
$\theta(°C)$	20.29	21.56	21.90	22.51
$\overline{w'w'}$ (m^2/s^2)	0.011	0.092	0.001	0.145
u_* (m/s)	0.074	0.223	0.020	0.225
$\overline{w'\theta'}(m°Cs^{-1})$	-0.0003	0.0343	-0.0002	0.0223

An increase in SST of about 8°C (6°C) over about 15 km (10 km) is seen across the GS front at the 8-m (33-m) level. The air potential temperature is greater for the higher level and its pattern of increase at the 33-m level is shifted eastward from that of the 8-m level by about 5 km. In spite of this shift, the air is still statically stable (Figure 14C). This could be due to the wind direction becoming more westerly as the flight altitude increases on the cool side of the SST front. This westerly wind at the 33-m level may push the cool air farther east, causing the location of the air potential temperature change to differ from that at the lower level. Also, the top of the forming unstable internal boundary layer may not reach the 33-m level until a few kilometers downstream of the SST change. The discrepancy between the two air temperature increases may also be due to the time change between the two levels of flights (about an hour's difference).

The surface temperature exhibits a secondary jump about 7 km west of the main temperature discontinuity (about 85 km offshore; Figure 13A), which we attribute to a "tongue" or pocket of the Gulf Stream extending into the cold water. The influence of this pocket is not seen at the 33-m level, but is seen in all 8-m level plots. Since these extensions of the Gulf Stream vary with time, it may be that the flight times are different enough to account for the lack of a pocket in the 33-m flights (33-m and 8-m runs are about an hour apart). The influence of the pocket could also be confined to only lower levels.

The wind direction at both altitudes is south-easterly on the warm side of the front. The wind speed is slightly stronger on the warm side of the boundary for both heights, but especially at the higher level. The stress vectors do not quite oppose the wind vectors in most cases presumably due to either sampling problems or differences between the wind and shear directions. At the 8-m level, the magnitude of the stress vector is positively correlated to sea surface temperature, including a turbulent bursting event about 7 km west of the GS boundary, seen in Figures 13A-D and 14A and C. This positive correlation is probably due to the influence of stability on the drag coefficient. At the 33-m level, however, the stress vector is negligible until about 93 km offshore (the region where the SST begins to increase) when the response to the warm GS begins, suggesting again that, on the cool west side of the front, a shallow stable boundary layer exists. This result is

supported by the vertical profile in Figure 15, showing a highly stable marine boundary layer on the west side of the GS front up to a height of about 200 m.

Friehe et al. (1991) studied the same SST front (southwest of Bermuda) as Khalsa and Greenhut (1989). For the day of flow from cold to warm water, on which the SST gradient was approximately the same as that in our unstable flow case, they found that, indeed, the low-level wind speed increased on the warm side of the front at the flight levels studied. In these runs, however, the surface stress decreased on the warm side and the upward heat flux remained approximately constant over the horizontal span of the SST front. They hypothesize that, on the warm side, reduced wind speed aloft accounted for the smaller surface stress and constant heat flux at lower levels.

Data are available 64 km south of the Bermuda front, over the warm water, which show that the stress is nearly identical to that on the cold side of the front; they conclude that the boundary layer had completely adjusted to the warmer surface waters by this distance from the front. Unfortunately, in our study, data were not taken very far over the warm water due to strong convection and cloudy conditions there; thus, we are unable to study adjustment farther downstream.

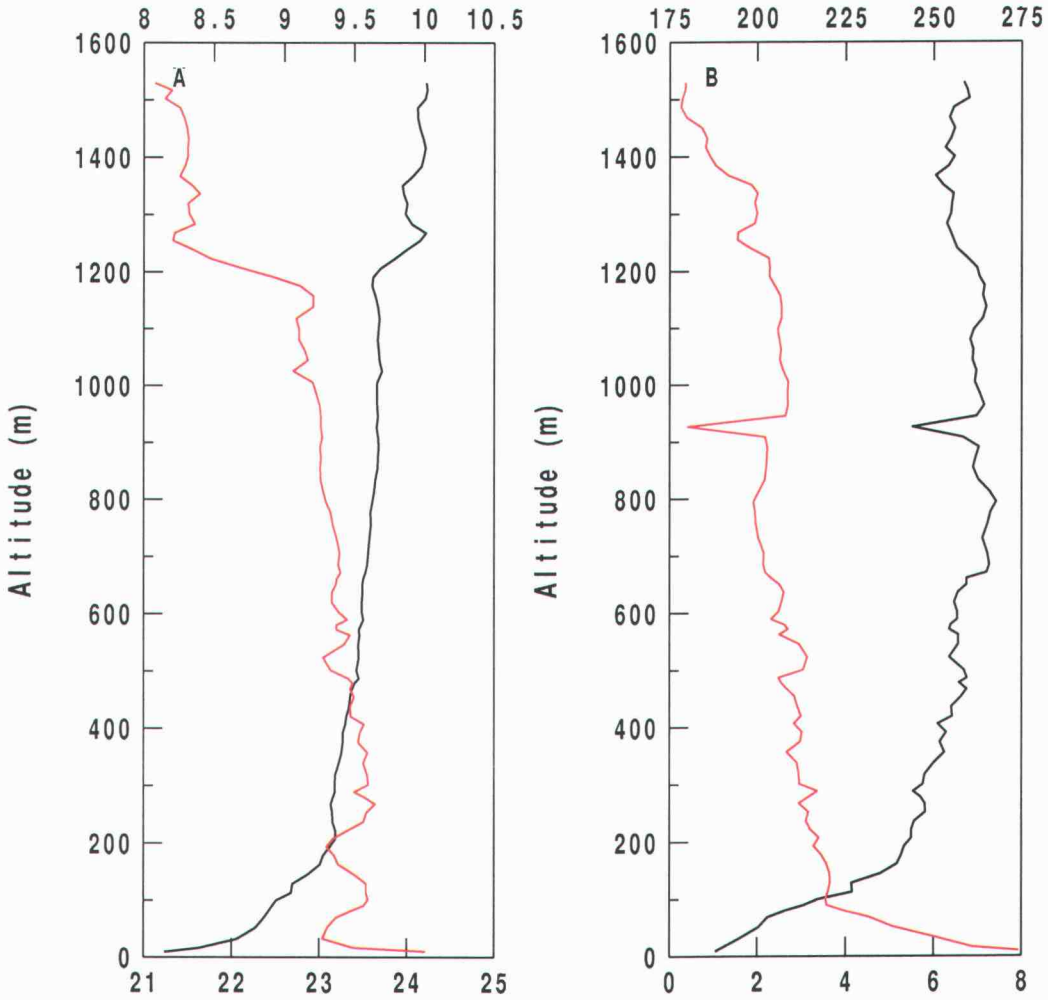

Figure 15: Vertical profile from a spiral sounding on 20 Nov. A) black line is $\theta(°C)$, red line is specific humidity (gkg^{-1}). B) black line is wind speed (ms^{-1}), red line is wind direction.

4.2.2.2 Momentum budget analysis

Table 3 shows our estimates for the terms in the momentum equation in the x-direction (Eq. 3). The horizontal temperature gradient at the upper level is apparently concentrated into more of a frontal zone, perhaps related to horizontal convergence at that level (Figs. 13A and 14C). As a result, the horizontal temperature gradient is difficult to estimate. Here we estimate it over the same spatial scale as the lower level for more meaningful comparison in the calculations of the $1/e$ folding depth (H_b) of the atmosphere and the horizontal temperature gradient a, which are required for the calculation of the thermal contribution to the horizontal pressure gradient across the front (Eq. 7). The large-scale pressure gradient term was evaluated for $H_b \sim 45m$ and $z_T = 200m$, the estimated top of the boundary layer from Figure 15. The net imbalance in the momentum equation for 20 Nov. predicts acceleration of the flow over time although the net imbalance may be dominated by errors.

Table 3. Estimated values of terms in the momentum equation for 20 November in units of ms^{-2}. Values are only accurate to the nearest order of magnitude. The stress divergence is presented on both the cold and the warm sides of the front.

$-\partial\overline{w'u'}/\partial z$ cold/warm	$-\alpha\partial p^*/\partial x$	$-\vec{v}\cdot\nabla u$	fv	$fv(z_T)$
$-2\times10^{-4}/-4\times10^{-4}$	9×10^{-4}	1×10^{-4}	3×10^{-4}	-4×10^{-4}

The stress divergence term is most vulnerable to error because the levels of the flux measurements were only 25 m apart. The measurements were

only taken to the height of 33 m on this day and may not adequately reflect the stress divergence throughout the internal boundary layer. Also, since the stress divergence typically increases toward the surface for stable conditions, estimating surface values from 8-m level data may underestimate the stress at this level.

The local thermally driven pressure gradient force is directed toward the warm water. The large thermally generated pressure gradient toward the east can be explained in the following way. Because of the temperature gradient over the SST front, there exists perturbation low pressure on the east and perturbation high pressure on the west side of the front at low levels. This hydrostatically induces a pressure gradient toward the east (Figure 16). According to our calculations, understanding that values are only accurate to their orders of magnitude, the local pressure gradient force is the largest term in the balance and largely governs the acceleration of flow toward the warm water.

The thermally-driven pressure gradient leads to concentrated horizontal convergence at about 97 km offshore at the 8-m level on the warm edge of the frontal zone and 102 km offshore at the 33-m level, where the air potential temperature is at its maximum for each level (Figure 14), and the total wind direction shifts from southwesterly to southeasterly. The center of the convergence appears to be where the sea surface temperature and air potential temperature cease to increase toward the east, that is, on the warm

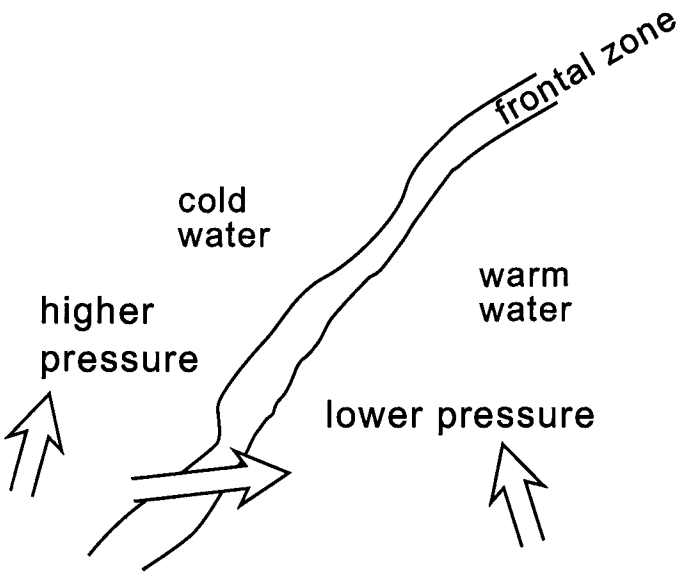

Figure 16: Idealized schematic of pressure gradient induced by the temperature discontinuity over the Gulf Stream front.

side of the frontal zone. To visualize the perturbation flow, the horizontal mean wind (averaged from 80 km offshore and eastward) is subtracted from the total wind at the 8-m level beginning at the west end of the SST front. These new wind vectors (Figure 17) show westerly flow between 88 and 97 km and easterly flow farther east, corresponding to significant horizontal convergence. This convergence corresponds to flow from the region of higher pressure toward the region of lower pressure. Eastward where the thermally-induced horizontal pressure gradient is very small, the convergence is no longer important. This horizontal structure is seen at the 33-m level as well but the pattern is shifted about 5 km to the east (not shown). Note that the actual flow (Figure 17) is more complex than the idealized schematic (Figure 16) possibly due to transient mesoscale motions and sampling problems.

4.2.3 Stable flow, 22 November

4.2.3.1 Spatial variation over the Gulf Stream

On 22 November (easterly flow), the SST decreases by about 3.5°C westward over a distance of about 3 km across the front. The air potential temperature at the 90-m (9-m) level, however, decreases by only about 0.3°C (0.5°C) and the decrease is spread over about 8 km, beginning at the east edge of the GS front, possibly due to weak mixing weakening the impact

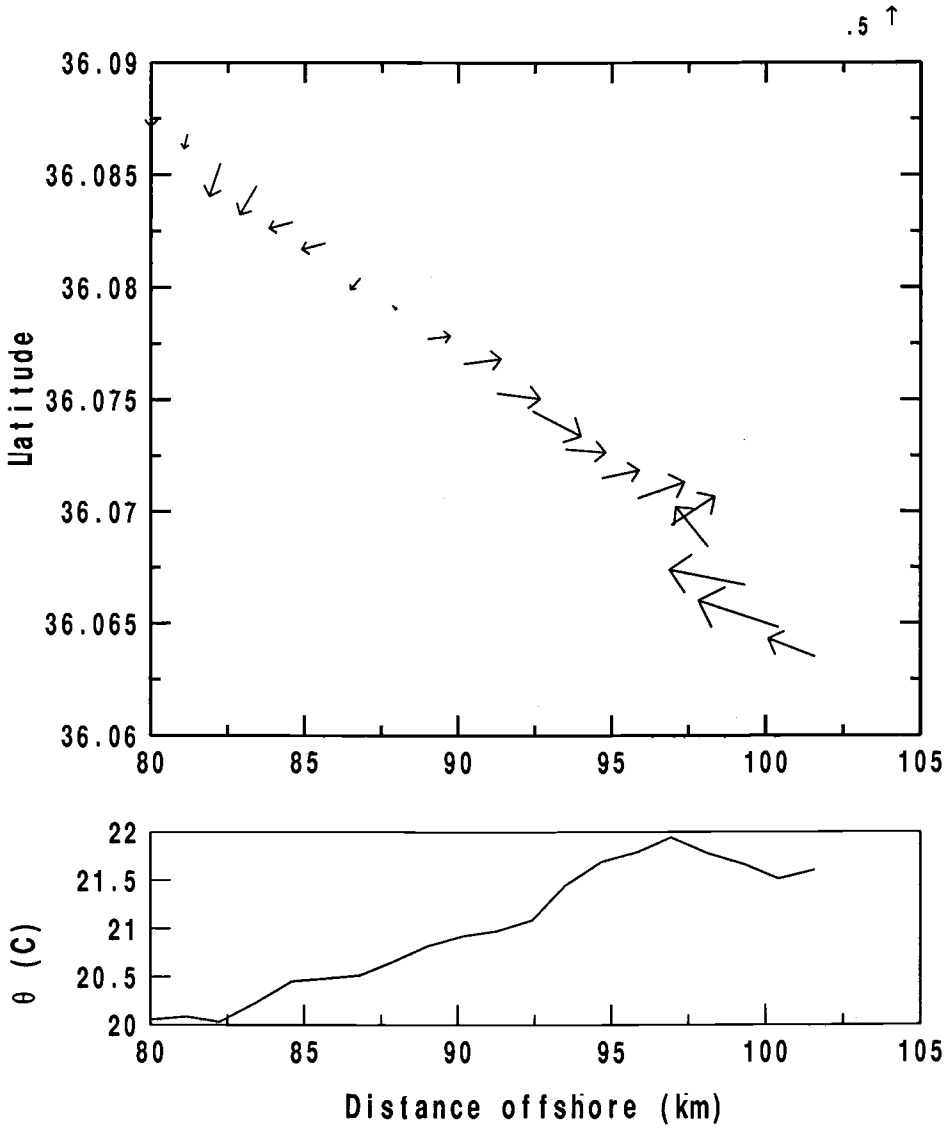

Figure 17: Wind vectors with mean wind subtracted, 20 November, 8-m level, and corresponding air potential temperature. The GS front begins at about 90 km offshore.

of the SST change. Apparently, the easterly flow advects turbulence from the warm side to the cool side of the front, resulting in slow decrease of the turbulence (Figures 18B-D).

The 90-m fluxes are highly variable, though they decrease slightly downstream. The low-level response is somewhat stronger than at the 90-m level. This could be due to greater wind speed aloft, causing more warm air advection at the 90-m level. Also, the forming stable internal boundary layer west of the GS front takes time to reach higher levels, delaying the response aloft to farther downstream.

For both heights, the heat flux is slightly upward (though $< 0.01°Cms^{-1}$) on the warm side and changes sign across the SST front. On both sides of the front, the air potential temperature is greater than the sea surface temperature, though the difference is much smaller over the warm water. The heat flux is an order of magnitude smaller than in the other two flow regimes and within random flux error estimates may in fact be negative on the warm side, as the air-sea surface temperature difference would suggest. The very small heat flux probably explains the slow response of the air temperature to the cooler water.

u_* is 65% (30%) greater on the warm side for the low (high) level. σ_w is 35% (50%) greater on the warm side compared to the cool side at the low (high) level. At both levels, $\overline{w'w'}$ increases considerably more than u_* (Table 4); however, u_* shows the sharpest response to the SST change, particularly at the low level, presumably due to the influence of stability on c_D (Figure

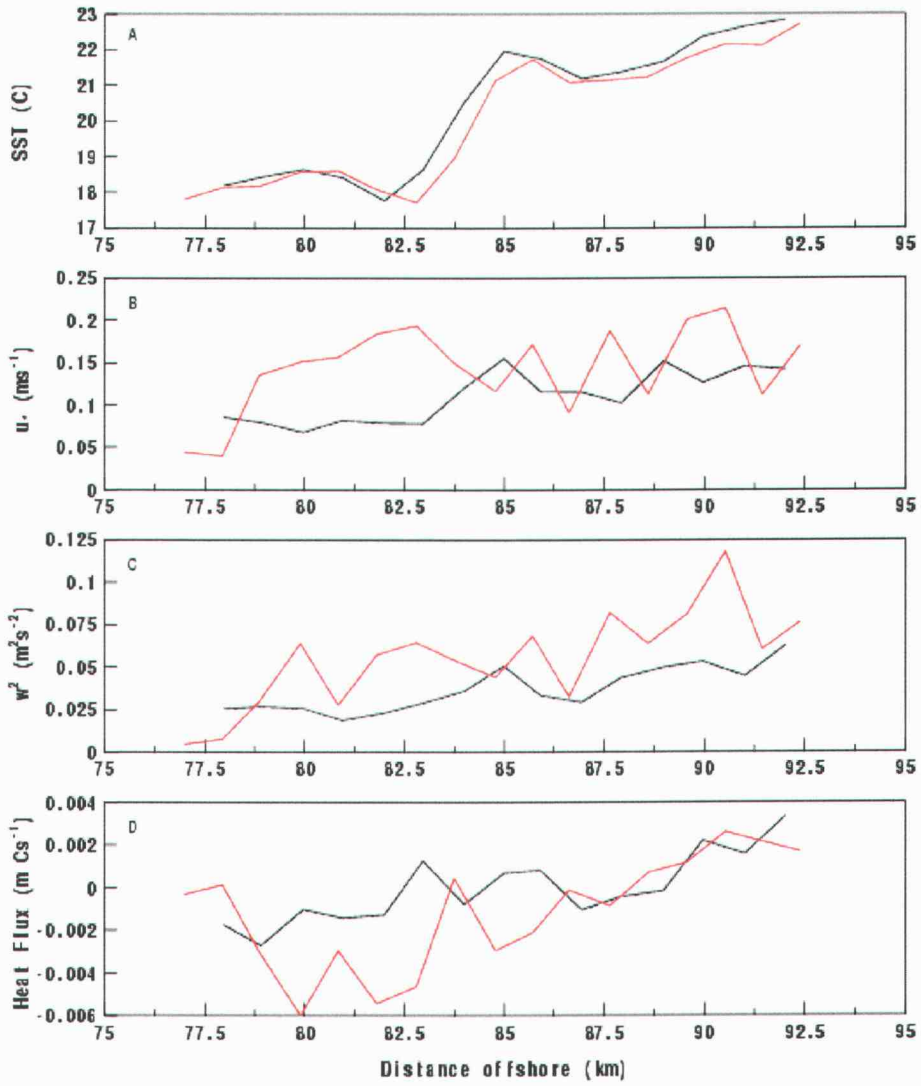

Figure 18: Composites for 22 November, 9-m (black) and 90-m (red) heights, for stable westerly flow.

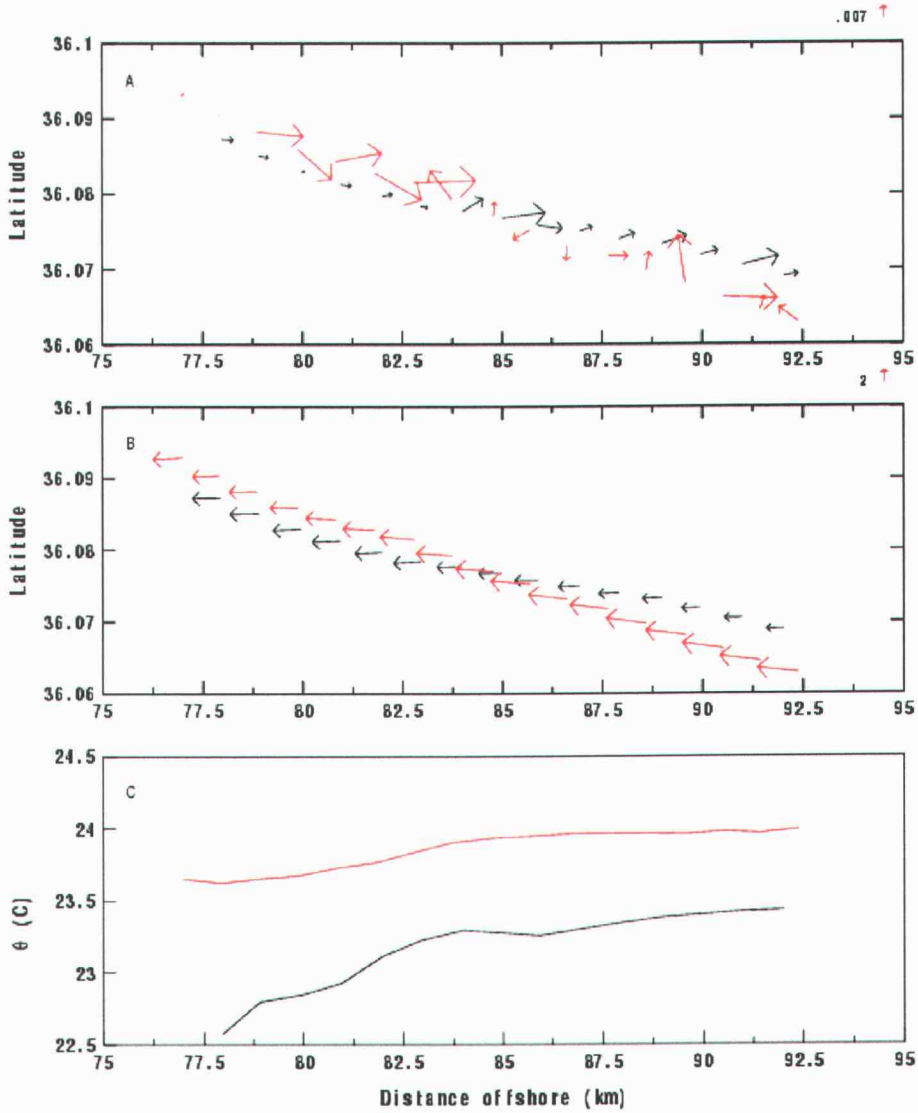

Figure 19: Composites for 22 November, 9-m (black) and 90-m (red) heights. A) stress vectors (legend shows size of 0.007 $m^2 s^{-2}$ vector), B) wind vectors (legend shows size of 2 ms^{-1} vector).

18B). Again, sampling and instrumental errors may significantly affect the fluxes, particularly on the cold side of the Gulf Stream.

Table 4. 9-m and 90-m level composites of 1-km means, 22 November.

	9-m level		*90-m level*	
	cold water	warm water	cold water	warm water
SST ($°C$)	18.29	21.98	18.22	21.74
$\theta(°C)$	22.85	23.36	23.69	23.97
$\overline{w'w'}$ (m^2/s^2)	0.024	0.045	0.032	0.073
u_* (m/s)	0.079	0.129	0.118	0.155
$\overline{w'\theta'}(m°Cs^{-1})$	-0.002	0.001	-0.003	0.001

The wind speed is about the same for both heights on the west side, but is smaller on the warm east side at the 9-m level and greater on the warm side at the 90-m level. The stress is very small at the low-level on the cool, west side of the front. The low-level wind acceleration accompanied by larger stress and turbulence aloft leads to the conclusion that an upside-down structure exists downwind of the GS front in this case. In these conditions, the low-level winds should accelerate due to stress convergence, as more momentum is coming down from aloft than is lost to the wave surface.

Figure 20, a spiral sounding taken on the cool, west side of the GS front, shows a new stable internal boundary layer forming downstream of the front up to about 40 m in height, with the warm residual boundary layer top at about 300 m in height, overriding the new cold boundary layer. The residual layer is well-mixed. The 90-m level in this case is thus above the forming

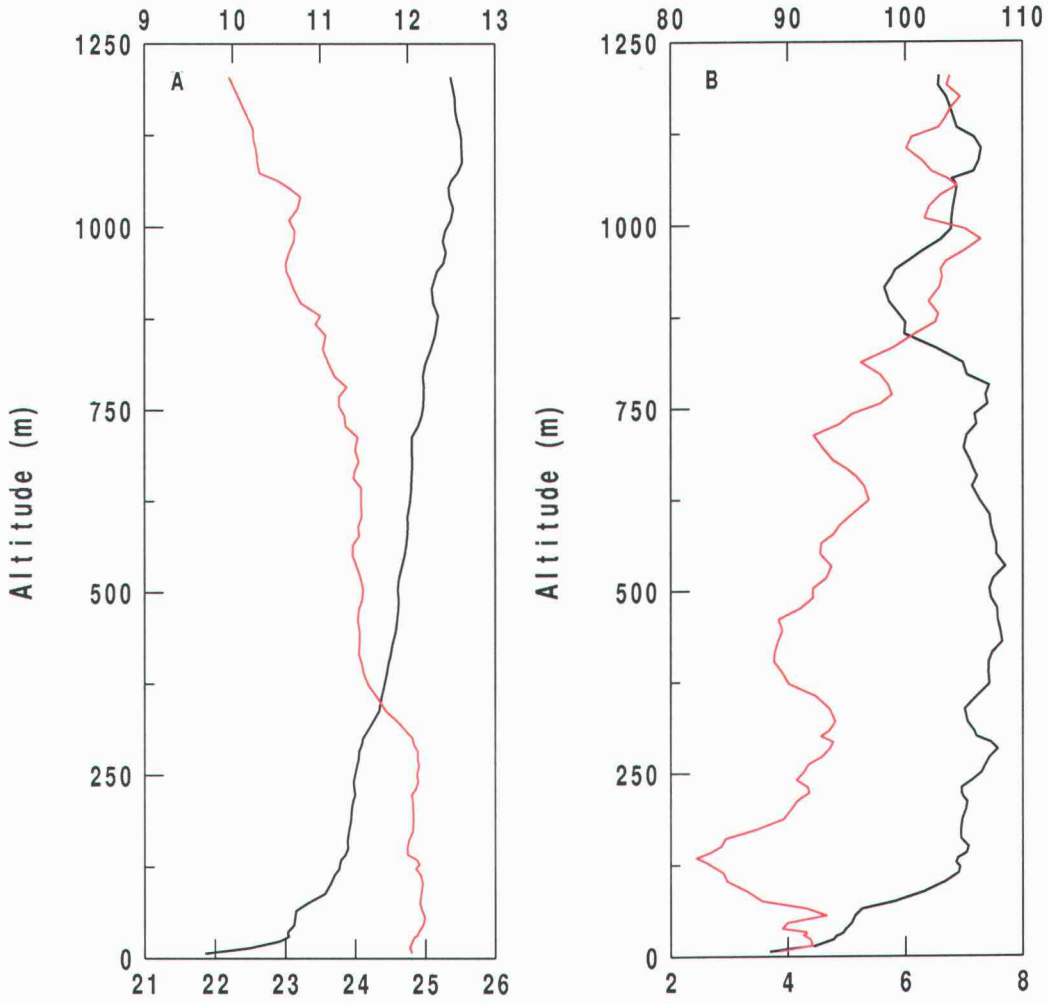

Figure 20: Vertical profile from a spiral sounding on 22 Nov. A) black line is θ(°C), red line is specific humidity (gkg^{-1}). B) black line is wind speed (ms^{-1}), red line is wind direction.

stable layer and could indeed be a source of turbulence bursting toward the surface as there is significant shear seen at the 90-m level in Fig. 20.

Friehe et al. (1991) studied the stable flow case from the Frontal Air-Sea Interaction Experiment (FASINEX). Our SST change was about twice as strong as the SST change in FASINEX on the stable flow day. They also found a change from an unstable to a stable heat flux regime as the air flowed from warm to cool water. Their data covered much more area, showing the heat flux gradually returning to zero far downstream from the front. The stress decreased by about a factor of 2 across the front, about the same as the Gulf Stream data of this study at the 9-m level. Friehe et al. (1991) discuss a monotonic decrease in surface stress and wind speed downwind of the front, which we see at the high-level but not at the low-level. Both studies agree that the heat flux magnitudes decrease substantially over the cold water, even more than in the unstable and parallel flow cases.

Koračin and Rogers (1990) used a one-dimensional, second-order closure scheme to model the response of the boundary layer to a SST front and corresponding ocean forcing (using the three-dimensional model presented in Yamada (1983)). With a substantial heat flux change from positive to negative across a front, they found that a stable internal boundary layer develops. The sea surface stress decreases due to the lessening of downward horizontal momentum transfer as the air near the surface becomes stable. They claim that this causes an increase in wind shear and vertical stress divergence; the wind slows at the low level, and increases at the higher level

due to reduced coupling to the surface frictional drag aloft. The decoupling from the surface stress leads to wind acceleration aloft. While the heat flux in our case changes sign across the front, the wind shear decreases. This could be due in part to a more pronounced SST front in our case ($-4°C$ compared to $-2.3°C$) or perhaps a less significant heat flux change, as the air temperature is greater than the SST even on the warm side of the GS. As shown here, stable cases are extremely difficult to model, as the downstream response to a surface change is unpredictable.

4.2.3.2 Momentum budget analysis

Table 5 shows the estimated values of the terms in the momentum equation (Eq. 3). The large-scale pressure gradient term is calculated from Eq. 7 for $H_b \sim 100m$ and $z_T = 300m$, the estimated top of the boundary layer, which was found from the vertical profile taken on this date on the cool side of the GS boundary (Figure 20). The momentum equation for this day predicts flow deceleration with time at the low level.

Table 5. Estimated values of terms in the momentum equation for 22 November in units of ms^{-2}. Values are only accurate to the nearest order of magnitude. The stress divergence is presented on both the cold and the warm sides of the front.

$-\partial\overline{w'u'}/\partial z$ cold/warm	$-\alpha\partial p^*/\partial x$	$-\vec{v}\cdot\nabla u$	fv	$fv(z_T)$
$-1\times10^{-4}/1\times10^{-4}$	2×10^{-3}	3×10^{-4}	-2×10^{-5}	-4×10^{-5}

The thermally generated pressure gradient term is the largest term in the momentum budget. Since this pressure gradient force is found in the transition zone, where the temperature gradient is large, we assume this force to be valid only within the 10 km taken to be the transition zone. The low-level wind increases in magnitude downstream despite the large local pressure gradient force acting against it.

The stress divergence term is the largest term to balance the small scale pressure gradient, but it is still an order of magnitude smaller. It acts to accelerate the flow on the cold side, as we predicted, due to the upside-down structure of this stable boundary layer, but it does not dominate the balance. This could be due to the large height difference in the layer. The lower level (9-m) is in the stable boundary layer, while the higher level (90-m) is well above it. We must also recognize that the stress divergence often decreases with height so that estimating the low-level stress as that of the surface would underestimate the stress there. In general, the stress divergence acts to oppose the flow as the stress decreases with height above the surface; since the turbulence is higher aloft in this case, the stress divergence accelerates the flow, hence the upside-down case does not follow traditional boundary layer theory.

The stress divergence on the warm side of the GS front is presented in Table 5 as well. Since there is too little sampling in the transition zone for accurate estimation there, we analyze the stress divergence on both sides of the front. The calculations in this case revealed that the stress divergence is

equal and opposite on either side of the GS transition zone. The stress does not change directions over the front, but the stress magnitude increases on the cool side aloft and decreases on the cool side near the surface. On the warm side, the usual case exists, in which the stress divergence opposes the flow; on the cool side, it acts as an accelerating force.

The horizontal advection term is large positive; vertical advection has been neglected in the momentum equation used in this study. Horizontal advection is included with the recognition that the vertical advection and horizontal advection terms are often of opposite sign, partially cancelling each other. For example, acceleration of the u-component of the wind in the downstream direction induces sinking motion, as demanded by mass continuity. This case corresponds to horizontal advection of weaker momentum and vertical advection of strong momentum (assuming the horizontal flow increases with height).

4.2.4 Predictability of the bulk Richardson number

Here we evaluate Eqs. 8-9 in terms of flow across the edge of the Gulf Stream. As there is no definitive up- and down-wind designation for 19 November, due to the wind direction being approximately parallel to the Gulf Stream boundary, no runs on this day are examined in terms of Richardson numbers. Since the wind direction is from the cold to the warm water (toward the east) on 20 November, the Richardson numbers are negative, corresponding

to unstable conditions (Table 6). On 22 November wind directions are from the east, corresponding to stable, positive Richardson numbers.

Table 6. Predictive Richardson number, bulk Richardson number, σ_w, and height for each run.

Date	Run	Height (m)	R_P	R_B	σ_w (m/s)
11/20	8	33	-9.95	-0.47	0.36
	9	33	-5.32	-0.21	0.39
	10	33	-6.94	-0.13	0.41
	15	8	-1.12	-0.13	0.29
	19	8	-1.33	-0.32	0.34
11/22	1	9	-0.03	0.03	0.15
	2	9	0.06	0.25	0.16
	3	9	0.08	0.37	0.19
	4	9	0.25	0.69	0.16
	5	9	0.31	0.92	0.16
	6	9	0.16	0.54	0.13
	7	9	0.16	0.55	0.17
	10	90	2.76	1.72	0.08
	11	90	2.82	1.86	0.12
	12	90	2.54	1.52	0.19
	13	282	6.04	5.95	0.22

On 20 November, the values of R_P show no apparent trend with time. R_P is considerably larger for the 33-m flights than for the 8-m flights; R_B shows no such time trend. In this case, the predictive Richardson number is an order of magnitude larger than R_B. This could be caused by the offshore wind on the west, cool side of the GS boundary increasing in magnitude significantly on the warm east side of the boundary. If the winds remained

the same over the boundary, R_B would be more likely to be closer to R_P. Predicting R_B from upstream conditions does not seem to be possible in unstable conditions.

On 22 November, the ratio of Richardson numbers remains relatively constant with time. The predictive Richardson number is consistently less than R_B at the 9-m level, most likely because the air temperature adjusts to the sea surface temperature downstream from the sea surface temperature discontinuity instead of remaining constant.

For higher level flights, both Richardson numbers increase by an order of magnitude and the predictive Richardson number is greater than R_B. This could be due to the fact that at higher levels, there is the chance that calculations of R_B are including air properties that are not part of the boundary layer; thus they are less coupled to surface-based processes. Also, the 10-m level may be too low to adequately represent the bulk stability of the boundary layer. At this level, the wind shear is in general greater than at higher levels. At about 280 m, well above the internal boundary layer, R_B and R_P both reach about 6, suggesting extremely stable conditions and little change in wind speed and θ over the SST discontinuity.

As seen in Figure 18B-C, u_* and $\overline{w'w'}$ on 22 Nov. are all greater at the 90-m level than at the 9-m level, suggesting an upside-down boundary layer structure, as described in Sections 4.1.2 and 4.2.3. The large magnitudes of the stress vector aloft (Fig. 19A-B) correspond to stress convergence, which would lead to low-level wind acceleration. Furthermore, R_B in most runs

is large in magnitude. Linear instability theory predicts that turbulence is generated for values of the gradient Richardson number less than 0.25, although turbulence is often observed at larger gradient Richardson numbers. While the relationship between the bulk and gradient Richardson numbers is not one-to-one, we assume it to be similar enough for comparison. We find R_B is greater than 0.25 in all but one case on 22 Nov., and much greater than 0.25 at levels at and above 90 m. These values of R_B suggest that there is little turbulence generated at these levels.

In order to visualize the dependence of the turbulence on stability, σ_w is analyzed with regard to its change with R_B (Figure 21). σ_w decreases sharply from neutral stability (R_B near zero) to weakly stable conditions and then becomes more independent of stability for $R_B > 0.25$. At higher stabilities, σ_w is more scattered. This relationship was noted in Mahrt (1987) and elsewhere.

4.2.5 SAR image analysis

The backscatter seen in satellite synthetic aperture radar (SAR) images is dependent on the ocean wave height with horizontal wavelengths on the order of centimeters, which is indicative of wind-induced surface stress; the magnitude of these waves is related to both ocean and atmosphere influences. Boundary layer convection has been shown to be evident in kilometer-scale (C-band) backscatter patterns of SAR images (Sikora et al., 1995; Winstead et al., 2002; Sikora et al., 1997), amongst other oceanographic and atmospheric

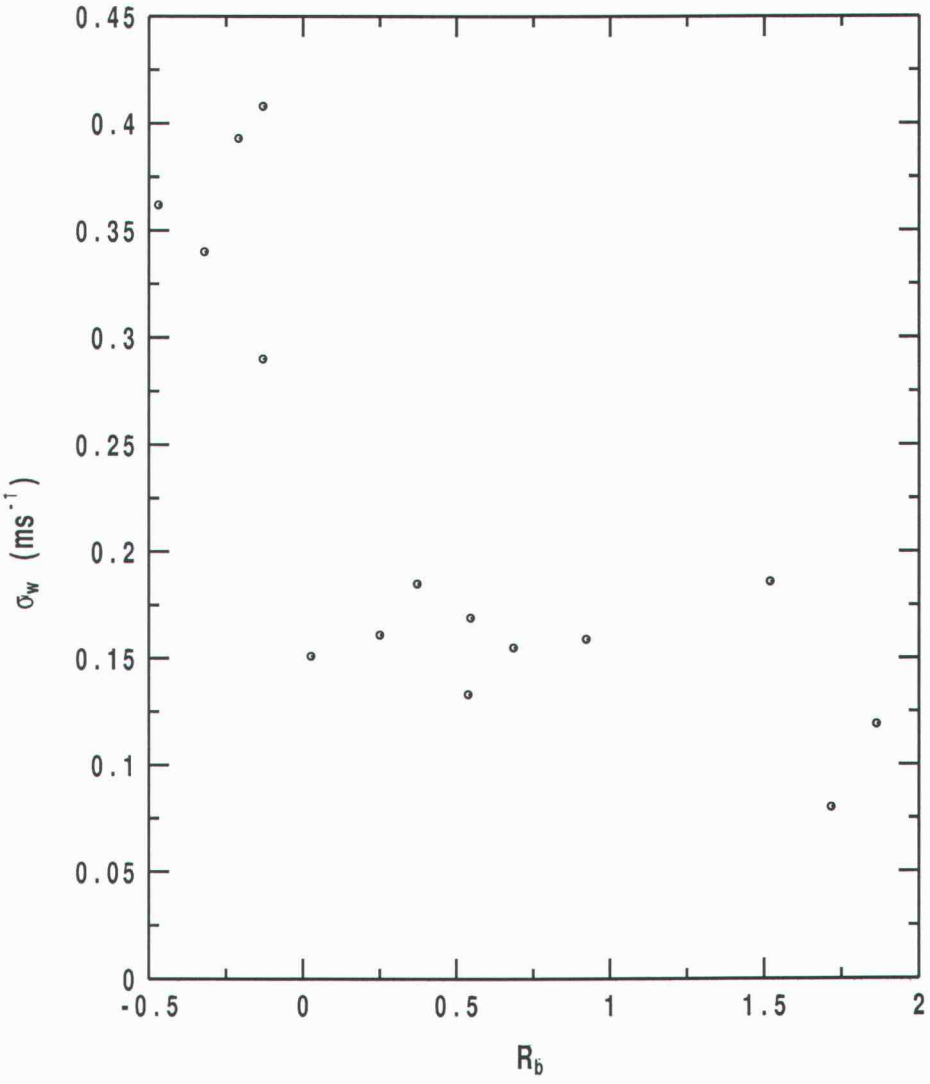

Figure 21: σ_w as a function of R_B for stable and unstable flow on 20 and 22 November. One point with large R_B is offscale.

phenomena, such as wave-current interactions, sea surface surfactant slicks, gravity waves, convective storms, and other mesoscale circulations caused by topography or sea surface temperature fronts (Young et al., 2000 and references therein). SAR imagery captures these surface roughness changes, with white/light colour signifying rougher surfaces, and dark/black colour representing calmer ocean surfaces. The rougher surfaces would be indicative of stronger winds and/or statically unstable conditions, where the sea surface temperature is greater than that of the air, while the less rough surfaces correspond to a region of statically stable conditions, presumably with the darker the colour, the more stable the conditions.

Under unstable conditions, enhanced turbulence creates greater sea surface roughness. Certain sea surface roughness patterns can be shown to be related to convection, a combination of updrafts and downdrafts, which is caused by buoyancy of turbulence when the sea surface temperature is greater than the air potential temperature. As downdrafts bring high momentum to the surface, the air accelerates and creates centimeter-scale surface waves and increases surface roughness. The opposite occurs for updrafts, with converging air at the surface reducing surface roughness. Since updrafts and downdrafts occur systematically in convection, this would lead to the assumption that these maxima and minima of surface roughness would in turn occur systematically. The footprint of convection upon the sea surface has

been shown to be one of mottling, with equal occurrence of up- and downdrafts creating equal occurrence of minima and maxima, respectively (Sikora et al., 1995; Sikora et al., 1997).

In addition, Sikora et al. (1995, 1997) conclude that a marbled backscatter pattern in SAR images corresponds to the occurrence of a statically stable boundary layer, as would typically be seen over the ocean especially in offshore flow. They hypothesize that the marbling occurs because of weak surface winds and/or the presence of sea surface surfactant slicks (SSSS). In this stable case, the SAR backscatter pattern is representing various oceanic phenomena and not the structure or stability of the marine boundary layer as significant turbulence is not present to alter the sea surface stress.

On 25 November at 1752 (EST), a SAR image was made over the Outer Banks and to the east, including the Gulf Stream boundary. The flow on this date is onshore (easterly). A marbled backscatter pattern is obvious near shore and extending east of the Outer Banks approximately 65 km offshore (to -75 °W; Figure 22). Just east of this offshore distance, however, the backscatter pattern changes to a more granulated texture. Although the image is quite distant, a vague mottled pattern is apparent in this region, suggesting convection east of the Gulf Stream boundary. In between the two patterns exists a somewhat disjointed area of black colour, signifying little, if any, sea surface roughness.

Figure 23 shows, on this same day, the sea surface temperature in the region of -75 °W compared to the SAR backscatter image. These plots show

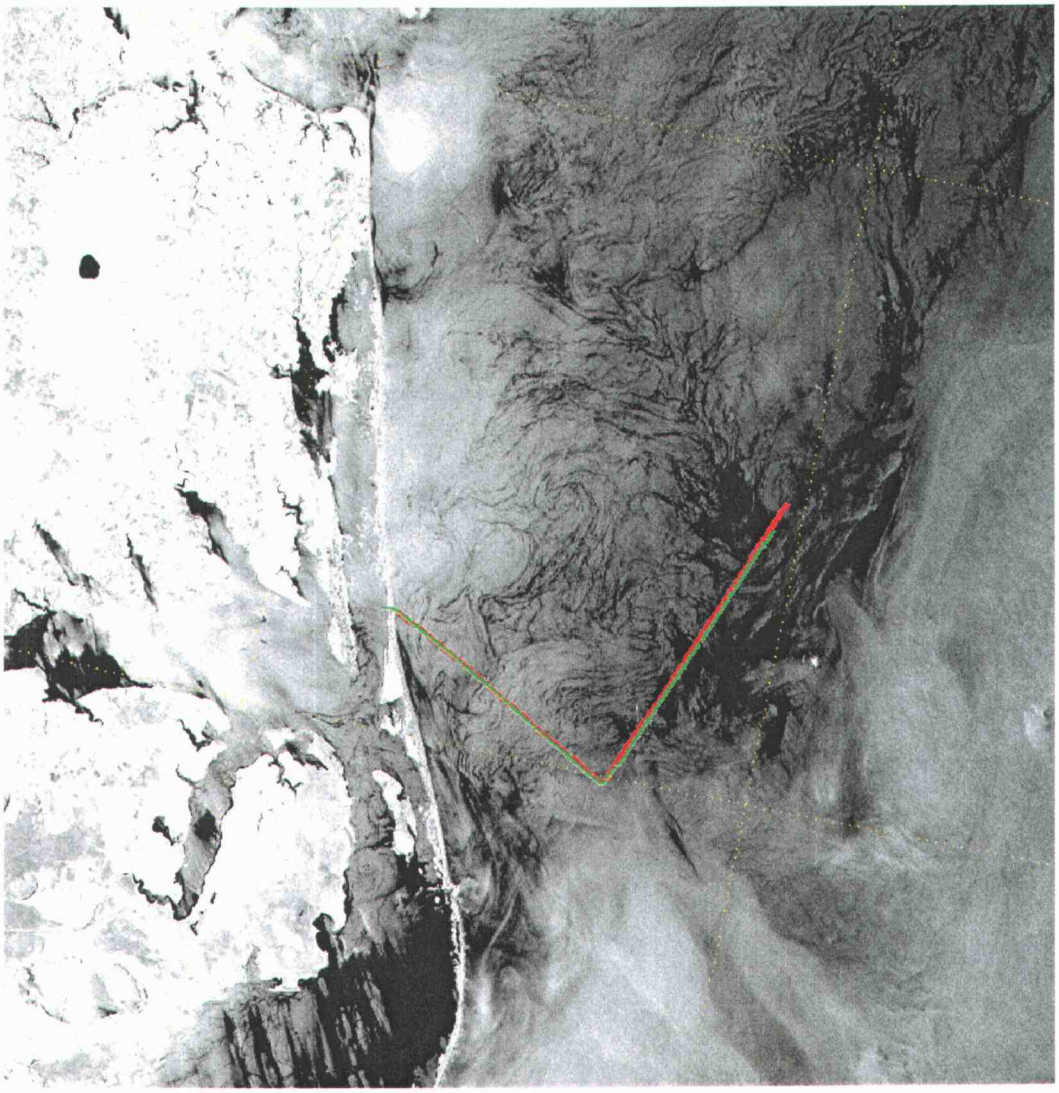

Figure 22: 25 November SAR image. LongEZ flight path is shown by the red line. © Canadian Space Agency 1999, received by the Canada Centre for Remote Sensing, processed and distributed by RADARSAT International.

a high level of agreement, with the SAR backscatter change at about 65 km offshore occurring in the same area as the SST change, which signifies the transition to the Gulf Stream. The marbled pattern on the cool side of the GS front corresponds to very little temperature variation in the SST plot.

This marbled backscatter pattern was studied in detail by Nilsson and Tildesley (1995) using SAR imagery taken east of Australia. They suggest that ocean backscatter is highly correlated with biological activity, particularly at higher latitudes. Thin surface films are formed by biological activity and have been found to reduce radar backscatter. They observed that spiral meanders, or narrow spiral lines, in the images are indicative of oceanographic flow rather than that of the atmosphere. Also, they found that the SST would have to suddenly fall by several degrees in order to change the surface stress enough to cause the observed drop in backscatter, even with small wind speed; thus, they conclude that the spiral lines are not likely to be caused by stability of the atmosphere. However, build-up of surfactants presumably requires small surface stress. Johannessen et al. (1993) considered several hypotheses for the possible cause of these spiral lines and concluded that the most probable one is sea surface surfactant slicks (SSSS) caused by the upwelling of organic matter into convergence zones. Hühnerfuss et al. (1977) found SSSS forming only when wind speeds were below 3-5 ms^{-1}. Higher wind speeds caused the SSSS to be removed from the surface via submersion.

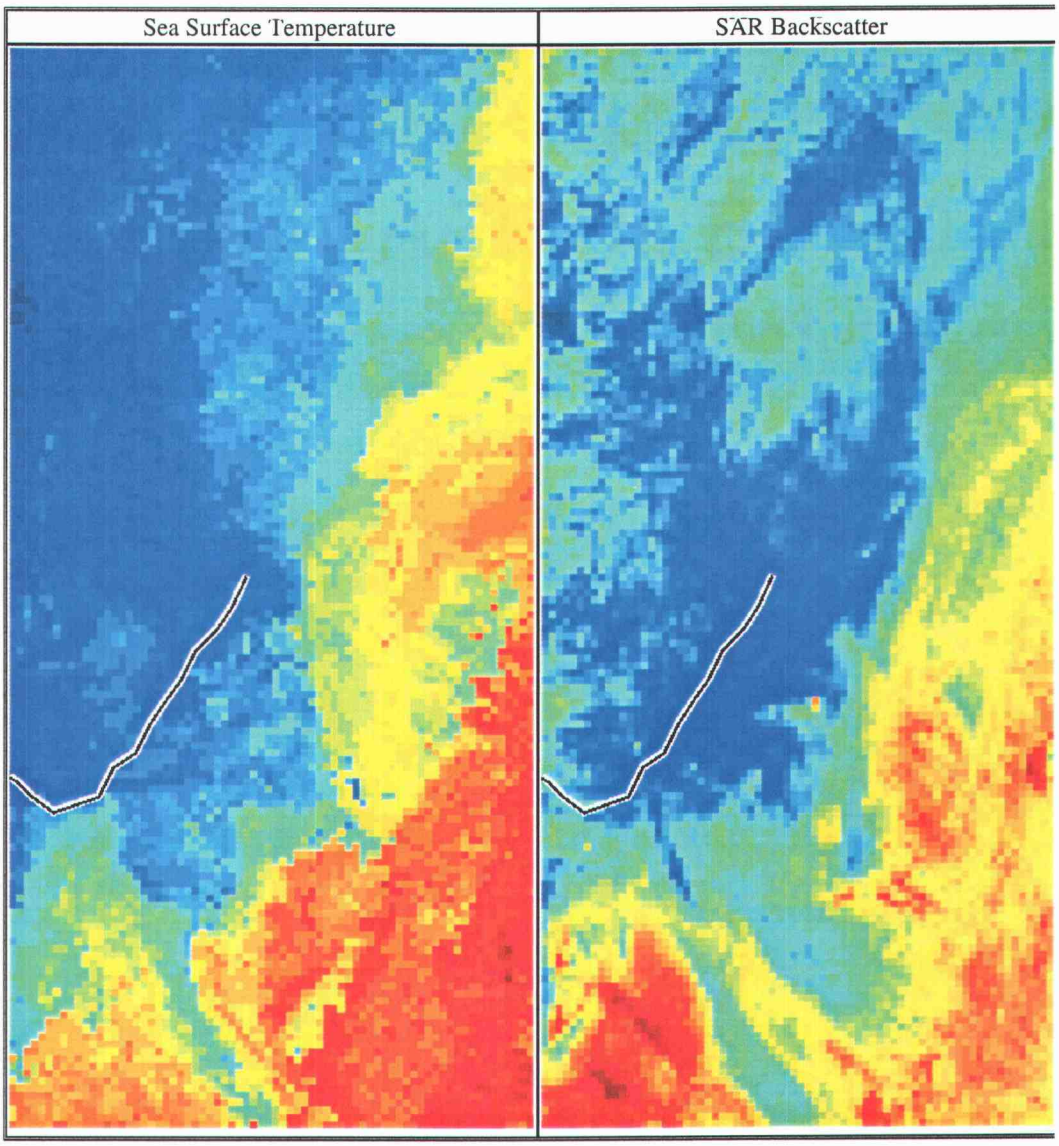

Figure 23: 25 November SAR image compared with an AVHRR SST image ending on the same day from Johns Hopkins Ocean Remote Sensing Group. The correlation is 0.77. LongEZ flight path is shown.

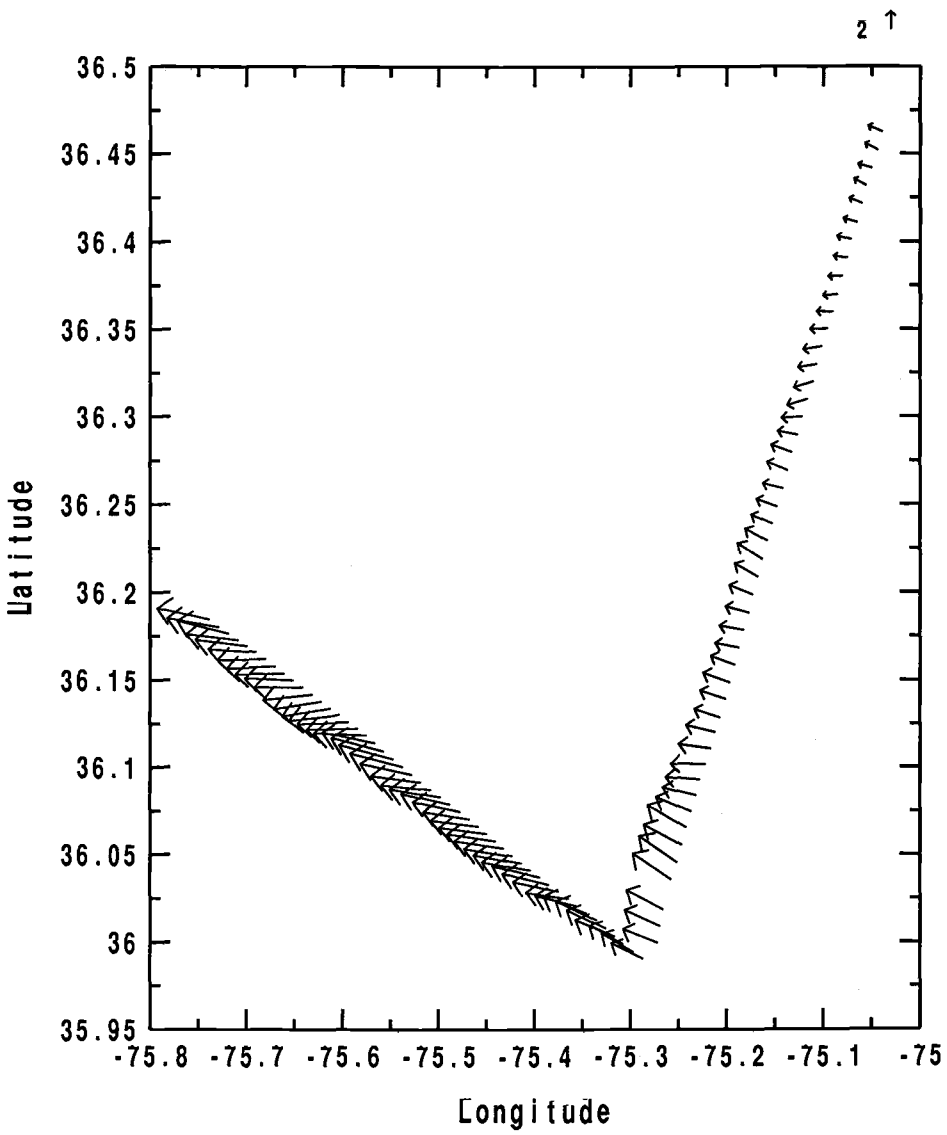

Figure 24: 25 November wind field (ms^{-1}), 30 m height, as observed by the LongEZ flight corresponding to SAR flight. Legend shows size of $2ms^{-1}$ vector.

Figure 22 shows evidence of narrow spiral lines as seen in the SAR images mentioned above. Figure 24 shows the wind field from the LongEZ flight taken during the SAR flight on 25 November (flight path is shown in Figures 22 and 23). Comparing Figures 22 and 24, it is obvious that more spiral lines occur as wind slows to speeds less than 5 ms^{-1}. This would suggest that these spiral lines seen as the marbled backscatter pattern are indeed caused by SSSS.

The dark regions in the SAR image (Figure 22) show up as regions of slight temperature increase in the SST plot of Figure 23. This may be where the transition zone occurs, where slight warming of the sea surface begins, but the temperature has not yet begun to exceed that of the air. The wind speed is approximately constant during the NW-SE leg of the LongEZ flight (Figure 24), at approximately 5 ms^{-1}, but decreases drastically during the SW-NE leg, reaching a value at or below 2 ms^{-1} for the last 15 km of the leg. The final wind speed at the NE corner of the flight is 1.6 ms^{-1}. Comparing the LongEZ wind data to the SAR image and SST plot, the gradual slowing of the wind speed corresponds to the region of little surface roughness, the black area between the mottled and marbled backscatter patterns. Mahrt et al. (2001b) and references therein describe the minimum wind speed for generation of surface waves as being in the range of 1.0 to 2.0 ms^{-1} from radar backscatter data. Kitaigorodski and Donelan (1984) also state that a smooth flow regime is estimated to occur at wind speeds less than 2.8 ms^{-1}.

These conditions occur for the most northerly 30 km of the LongEZ SAR flight, indicating that, indeed, the surface is calm and these above estimates apply to this data as well.

With flow of warm air over cooler water, the turbulence collapses near the surface, as indicated by the dark region in Figure 22 as well as the marbled area to the west. LongEZ eddy correlation measurements taken in correspondence to the SAR image (track shown in Figures 22 and 23) indicate that the friction velocity is everywhere less than about 0.05 ms^{-1}, except for two local bursts of turbulence, even in the regions of the flight where the wind speed exceeds 6 ms^{-1}. Similarly, the vertical velocity variance is extremely small (Figure 25). Because of random flux error and possible instrument noise, these values may be zero within error estimates. Because of the stratification due to warm air advection over cool water, the turbulence collapses even when winds are not weak. This collapse is predicted by the lack of SAR return associated with only very small momentum flux to the sea surface (very small u_*).

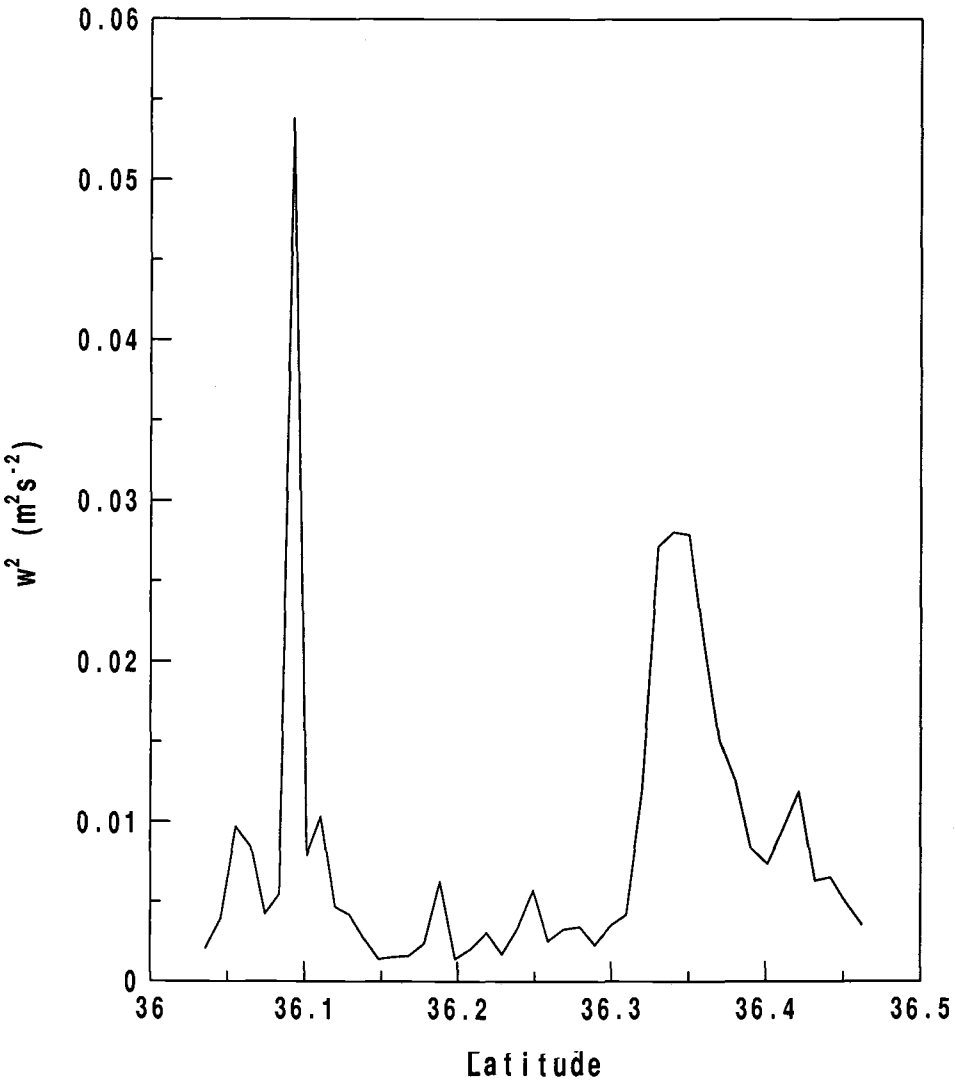

Figure 25: $\overline{w'w'}$ as a function of latitude in the region of little SAR backscatter just west of the Gulf Stream, 25 November.

5. GROWTH OF THE INTERNAL BOUNDARY LAYER OVER SURFACE DISCONTINUITIES

This sub-study analyzes the growth of the internal boundary layer over sea-surface discontinuities, including flow from water over land and flow between cool water and warmer water, such as over the Gulf Stream boundary east of the Outer Banks. These results are compared with results of previous studies including a study of land breezes. Several flights were made perpendicular and parallel to the coast at different levels and at different distances from shore in order to study the horizontal and vertical structure of the boundary layer, both over the water and over the land. Wind directions varied according to flight, however the wind direction is generally from the southwest, corresponding to offshore flow.

5.1 ANALYSIS

Mahrt (1996) and references therein describe the growth of the internal boundary layer, the layer of modified air that develops as a result of a change in surface characteristics. They present the following equation to describe internal boundary layer growth (Brutsaert, 1982):

$$\frac{dh_b}{dx} = C\frac{\sigma_w}{U} \tag{10}$$

where h_b is the depth of the internal boundary layer, x is the distance downstream from the surface discontinuity, C is a nondimensional growth rate coefficient, U is the wind speed evaluated at the top of the layer, and σ_w is

the standard deviation of the turbulent fluctuations of vertical velocity. This slope is estimated to be proportional to the slope of a hypothetical parcel of air advected at wind speed U, and rising at speed σ_w (Mahrt et al., 1994). Related forms of Eq. 10 replace σ_w with u_*. These relationships provide a much simpler, but presumably less accurate, description of internal boundary layer growth. Brutsaert (1982) predicts a $0.01m/m$ growth rate for an internal boundary layer with neutral stratification.

5.2 RESULTS

The growth of the internal boundary layer as the air flows from Abermarle Sound over the Outer Banks is analyzed here in order to quantify the depth of the boundary layer when it reaches the Atlantic Ocean on the east side of the barrier island. Using the thermocouple data from the tower at Duck, the height of the boundary layer on 18 Mar. and 04 Dec. was found to be about 25 m at the tower's location (Figure 21 shows the profile on 18 Mar.). Aircraft data just offshore of the Outer Banks showed an IBL height of about 200 m (110 m) on 18 Mar. (04 Dec.) downstream from much wider land (not shown). Vickers et al. (2001) also find the depth of the land-based convective IBL to be about 200 m using data measured approximately 5 km downstream on 18 Mar. Analysis of Eq. 10 for 18 Mar. and 04 Dec. resulted in values of C ranging from 0.5 to 1.7. On 18 Mar., the aircraft profile at the coast gives a C value of 1.7 ($dh_b/dx = 0.04m/m$), while the tower data suggest that C is 0.7 ($dh_b/dx = 0.02m/m$). On 4 Dec., the results are both similar to the

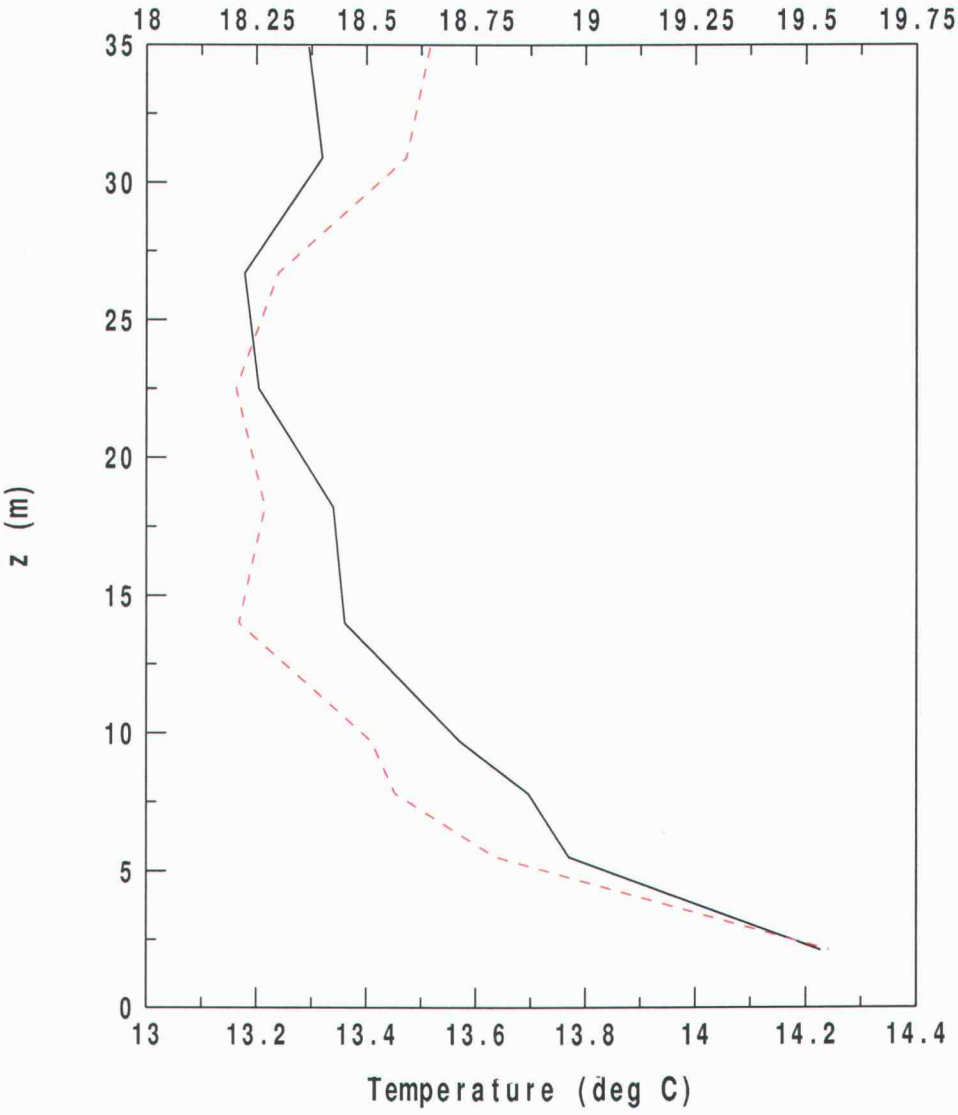

Figure 26: Temperature profile on 18 March, taken from the tower at Duck. Solid line, 08:30 (EST); dashed line, 11:30 (EST).

tower results of 18 Mar. These calculations predict that the growth of the internal boundary layer proceeds at a rate on the order of $0.01m/m$ on both days.

The tower data were taken at Duck, where the land is approximately 1.5 km wide, while the aircraft data were taken downstream from land that is up to 5 km wide. The differences in upstream land width between the aircraft and tower datasets lead to differing values of growth rates for each method of measurement. Also, the tower at Duck was placed downstream from small roughness (grass, low shrubs); at most other points on land, the upstream roughness is greater due to urban development and trees. This may be responsible for the differing quantities derived for the growth rates between the datasets as well. Furthermore, different surface heating could lead to differences in growth rate between the two days studied even though the influence of surface heating is indirectly included through σ_w, which includes both the influences of buoyancy generation and shear generation of turbulence. However, σ_w may not accurately represent these influences on the growth of the internal boundary layer.

The internal boundary layer growth also depends on the stratification above the internal boundary layer. Stronger stratification above the growing internal boundary layer reduces the growth rate of an internal boundary layer. In addition, mean sinking motion (rising motion), possibly due to flow acceleration (deceleration), leads to slower (faster) growth of the internal boundary layer (Vickers et al., 2001).

The maximum width over which the IBL can develop is greater for the aircraft data compared to the tower. Since the growth rate often decreases in the downstream direction, the greater fetch would suggest a smaller value of C and dh_b/dx for the aircraft. For example, in Vickers et al. (2001), the aircraft on 14 November is found to intersect the forming unstable boundary layer at 110 m altitude about 1100 m east of the western edge of the Outer Banks. This gives an internal boundary growth rate of $0.1m/m$ near the surface discontinuity, an order of magnitude greater than that found by either the aircraft or the tower on both 18 March and 04 December at the east edge of the Outer Banks. Thus, since the tower values are actually less than those of the aircraft, we conclude that the smaller values of C at the tower must be due to small surface roughness upstream.

Mahrt et al. (1994) evaluate Eq. 10 and determine C values of 0.9 and dh_b/dx of about $0.15 - 0.2m/m$ for the California Ozone Deposition Experiment (CODE); this calculation used data from flights during which air flowed from an irrigated field to a warmer, dry field, a case of unstable flow. Mahrt (2000) evaluates Eq. 10 for Twin Otter aircraft measurements of warm air flowing over a cooler Boreal lake (Candle Lake) and found C to be 0.15, and dh_b/dx about $0.004m/m$. The low growth rate may have been due to near collapse of turbulence close to the cool lake surface and extremely small surface roughness.

Table 7. Growth rate and nondimensional growth rate coefficient for each case, presented with its flow regime and up- and down-stream surface type. (T) denotes tower data, (A) denotes aircraft data, (GS) denotes Gulf Stream aircraft data, C Water is cool water, W Water is warm water.

Project	Up Sfc	Dn Sfc	dh_b/dx	C
03/18 (T)	Water	Land	0.02	0.7
03/18 (A)			0.04	1.7
SHOWEX 12/04 (T)			0.02	0.5
12/04 (A)			0.02	0.7
11/20 (GS)	C Water	W Water	0.01	0.2
CODE	Moist Sfc	Dry Sfc	0.15-0.2	0.9
Candle Lake	Land	Water	0.004	0.15

The growth of the internal boundary layer over the SST front at the Gulf Stream boundary is studied on a day of unstable westerly flow, with air flowing from over cool water to over warmer water. On 20 November, the aircraft intersects the top of the forming unstable internal boundary layer at the 33-m level about 3.5 km downstream from the surface heterogeneity, where the surface temperature is seen to begin to increase (Figure 13A-C). This suggests that the slope of the growth of the IBL is about $0.01 m/m$. Backing out C from Eq. 10 gives a value of 0.2. All above-mentioned IBL growth parameters are shown for comparison in Table 7.

Both SHOWEX datasets have a predicted growth rate of the same order of magnitude as the neutral stratification prediction of Brutsaert (1982), while in CODE it is an order of magnitude higher. Mahrt et al. (1994) claim this is due to strong heating and weak wind speeds during the CODE runs; also,

this is the only case studied here in which both the up- and down-stream surfaces are land. The only stable flow case, Candle Lake, shows by far the smallest growth rate, at least an order of magnitude less than all others shown. These findings bring much surprise, as theoretically σ_w should take into account surface roughness (z_0), causing the growth rate to not vary with surface roughness.

It is because of the dependence of dh_b/dx on wind speed and buoyancy that we conclude that C is better for intercomparison, as it is a nondimensional growth rate parameter. However, the coefficient C is still considerably smaller in the cases with water as the downstream surface than the cases with downstream land, again suggesting that surface roughness strongly influences the growth rate of the internal boundary layer.

6. CONCLUSIONS

The width of land that air passes over before flowing over water has a strong effect on the evolution of the turbulence over the water. This result is similar to that of Winstead and Mourad (2000) and Winstead and Young (2000), who conclude that along-shore terrain variations create varied signatures on the water surface thought to be related to sea surface stress. Here the effect of land width can be seen at all observation levels, up to the boundary layer top. The influence of along-shore variations decreases with sea fetch as the turbulence decays and horizontal diffusion smoothes horizontal variations. That is, the footprint that the measurements capture farther from shore includes a wider swath of land, and thus is not specific to the land fetch directly upstream from the measurement. The decrease in turbulence offshore is also related to the stability of the flow; days with stronger stability over the water show smaller sea surface flux values.

As found in Sun et al. (2001), the large momentum flux near-shore is due to the advection of momentum flux from the upstream land surface; farther from shore, the effect of advection is seen to decrease dramatically. As such, advection and the decay of turbulence offshore, governed by the structure of the turbulence in the upstream boundary layer, are the primary causes of the spatial structure of the fluxes. Vickers et al. (2001), in fact, evaluate the terms in the equation of motion for the mean wind for three offshore flow cases in SHOWEX (including 18 Mar.). In all cases, horizontal advection is the largest term in the first few kilometers offshore; the horizontal pressure

gradient, vertical advection, and vertical flux divergence terms are estimated to collectively balance the large horizontal advection in these cases.

A maximum in the momentum flux is seen aloft just offshore of the Outer Banks (Vickers et al., 2001). This finding does not follow traditional boundary layer theory, in which turbulent fluxes are expected to decrease with height. The higher-level air becomes partially detached from the surface and the low-level turbulence decreases due to buoyancy destruction. This creates the momentum flux maximum that occurs well above the surface as described in Smedman et al. (1993, 1995).

On all days studied, the atmospheric flow is strongly influenced by the horizontal temperature variation across the GS boundary. The study of airflow and turbulence data across surface temperature heterogeneities, such as the Gulf Stream boundary, provides valuable analysis opportunities for contrasting flow regimes. Unstable flow is well-understood, with upward buoyancy flux creating an internal boundary layer that grows in the downstream direction. Stable flow, however, is more of an enigma, as the downstream structure is unpredictable and follows no apparent pattern from one day to the next. A turbulent internal boundary layer may or may not form, and its structure, should one form, is highly variable.

On 20 and 22 Nov., the days during which conditions were conducive to analysis of the momentum budget equation, the thermally generated pressure gradient force directed toward the warm side of the GS boundary was seen to be the largest term. This term was also shown to be considerably

greater than the large-scale pressure gradient term on both days. This local thermally-induced pressure gradient dominates the momentum budget and acts to accelerate the westerly flow (20 Nov.) and decelerate the easterly flow (22 Nov.).

On 20 Nov., wind convergence occurs at both levels in the region of the GS front. We find that this is due to the thermally generated pressure gradient force. Both our analysis of wind vectors with the mean wind removed (Fig. 17) and the momentum budget analysis show that a strong local pressure gradient force drives deceleration in the frontal transition zone. Vertical stress convergence at the surface could contribute to the horizontal convergence at the front, but it is found to have a considerably smaller magnitude than the local pressure gradient term.

On 22 Nov., the stress divergence term acts to accelerate the flow, rather than acting as a drag. This is caused by the upside-down internal boundary layer structure on this day. The weak low-level turbulence is smaller than that at the 90-m level. While the stress convergence acts to accelerate the flow, it is an order of magnitude smaller than the local pressure gradient term, which is opposing the flow, and thus the flow decelerates.

The predictive Richardson number is somewhat useful for predicting the pattern of the downstream response to a surface discontinuity, especially in the stable case; however, for the flight levels studied, the predicted bulk Richardson number required a calibration coefficient of about 3.5 at 9-m heights in the stable case. A similar time dependence is seen for both

Richardson numbers. At the 90-m level in the stable case, the calibration coefficient decreases to 0.6. At higher levels the flow becomes less related to surface properties, particularly for stable conditions, reducing the utility of any Richardson number at these levels. Richardson numbers in the unstable conditions studied here do not show a sufficiently consistent pattern to estimate a calibration coefficient.

In the stable case, on 22 Nov., the bulk Richardson number was consistently greater than 0.25, the linear theoretical upper limit of the gradient Richardson number for the existence of turbulence. This would suggest stable conditions at these levels, which are seen in vertical profiles as well as in the study of horizontal variation across the GS. The stability suggested by the bulk Richardson number increases with altitude.

SAR imagery provides a useful complement to low-level data collection experiments. We see evidence of convection and stable conditions in the different backscatter patterns on 25 Nov. and a considerable change in the SAR return in the area of the GS front ($-75°$W). The comparison of simultaneous LongEZ wind and eddy correlation data with the SAR image shows agreement between the two data sources. The marbling pattern in the SAR image has been shown to be indicative of stable conditions, weak surface stress, and/or sea surface surfactant slicks (SSSS) (Sikora et al., 1995; Sikora et al., 1997; Nilsson and Tildesley, 1995). LongEZ data show small wind speed, u_*, and vertical velocity variance in areas of minimal SAR return, indicating relatively stable conditions. Spiral lines in the SAR image are indicative of

SSSS, the upwelling of organic materials to the ocean surface which dampen surface waves (Johannessen et al., 1993), and are shown to occur at wind speeds less than 3-5ms^{-1} (Hühnerfuss et al., 1977), which occur during most of the corresponding LongEZ flight. While SAR imagery seemingly does not constitute a reliable sole data source for analysis, it can be useful in complementing or supplementing surface-level experiments.

The growth of internal boundary layers is affected by not only buoyancy and wind shear, but by surface roughness. The growth situations we evaluate and reference show significantly different normalized growth rates for varying up- and down-stream surfaces. The situations with downstream water (land) had consistently smaller (greater) growth rates. While the inclusion of σ_w in the internal boundary layer growth rate formulation should take into account varying surface roughness and buoyancy, we find that enough variability exists in the growth rates to suggest that surface roughness plays a stronger role than formerly thought.

BIBLIOGRAPHY

Brutsaert, W.H.: 1982, *Evapotranspiration into the Atmosphere-Theory, History, and Applications.* D. Reidel Publishing Company, Dordrecht, 299pp.

Crescenti, G.H., T.L. Crawford, and E.J. Dumas: 1999, Data Report: LongEZ (N3R) Participation in the 1999 Shoaling Waves Experiment (SHOWEX) Spring Pilot Study, NOAA Technical Memorandum ERL ARL-232, Silver Spring, MD, 86pp.

French, J.R., G.H. Crescenti, T.L. Crawford, and E.J. Dumas: 2000, LongEZ (N3R) Participation in the 1999 Shoaling Waves Experiment (SHOWEX), NOAA Data Report OAR ARL-20, Silver Spring, MD, 51pp.

Friehe, C.A., W.J. Shaw, D.P. Rogers, K.L. Davidson, W.G. Large, S.A. Stage, G.H. Crescenti, S.J.S. Khalsa, G.K. Greenhut, and F. Li: 1991, 'Air-Sea Fluxes and Surface Layer Turbulence Around a Sea Surface Temperature Front', *J. Geophys. Res* **96**, 8593-8609.

Horst, T.W. and J.C. Weil: 1994, 'How far is far enough?: The fetch requirements for micrometeorological measurement of surface fluxes', *J. Atmos. Oceanic Technol.* **11**, 1018-1025.

Hühnerfuss, H., W. Walter, and G. Kruspe: 1977, 'On the variability of surface tension with mean wind speed', *J. Phys. Oceanogr.* **7**, 567-571.

Johannessen, J.A., L.P. Røed, and T. Wahl: 1993, 'Eddies detected in ERS-1 SAR images and simulated in reduced gravity model', *Int. J. Remote Sens.* **14**, 2203-2213.

Khalsa, S.J.S. and G.K. Greenhut: 1989, 'Atmospheric Turbulence Structure in the Vicinity of an Oceanic Front', *J. Geophys. Res.* **94**, 4913-4922.

Kitaigorodski, S. and M. Donelan: 1984, 'Wind-wave effects on gas transfer, in Gas Transfer at Water Surfaces', edited by W. H. Brutsaert and J. Jirka, D. Reidel Publishing Company, Norwell, MA, 147-170.

Koračin, D. and D.P. Rogers: 1989, 'Numerical simulations of the response of the marine atmosphere to ocean forcing', *J. Atmos. Sci.* **47**, 592-611.

Mahrt, L.: 1987, 'Grid-Averaged Surface Fluxes', *Mon. Wea. Rev.* **115**, 1550-1560.

Mahrt, L.: 1996, 'The Bulk Aerodynamic Formulation Over Heterogeneous Surfaces', *Boundary-Layer Meteorol.* **78**, 87-119.

Mahrt, L.: 2000, 'Surface Heterogeneity and Vertical Structure of the Boundary Layer', *Boundary-Layer Meteorol.* **96**, 33-62.

Mahrt, L., J. Sun, D. Vickers, J.I. MacPherson, J.R. Pederson, and R.L. Desjardins: 1994, 'Observations of Fluxes and Inland Breezes over a Heterogeneous Surface', *J. Atmos. Sci.* **51**, 2484-2499.

Mahrt, L., D. Vickers, J. Edson, J. Wilczak, J. Hare, and J. Hojstrup: 2001a, 'Vertical structure of offshore flow during RASEX', *Boundary-Layer Meteorol.* **100**, 47-61.

Mahrt, L., D. Vickers, J. Sun, T. Crawford, G. Crescenti, and P. Frederickson: 2001b, 'Surface stress in offshore flow and quasi-frictional decoupling', *J. Geophys. Res* **106**, 20,629-20,639.

Nilsson, C.S. and P.C. Tildesley: 1995, 'Imaging of oceanic features by ERS 1 synthetic aperture radar', *J. Geophys. Res.* **100**, 953-967.

Sikora, T.D., G.S. Young, R.C. Beal, and J.B. Edson: 1995, 'Use of Spaceborne Synthetic Aperture Radar Imagery of the Sea Surface in Detecting the Presence and Structure of the Convective Marine Atmospheric Boundary Layer', *Mon. Wea. Rev* **123**, 3623-3632.

Sikora, T.D., G.S. Young, H.N. Shirer, and R.D. Chapman: 1997, 'Estimating Convective Atmospheric Boundary Layer Depth from Microwave Radar Imagery of the Sea Surface', *J. Appl. Met.* **36**, 833-845.

Smedman, A., H. Bergström, and U. Högström: 1995, 'Spectra, Variances and Length Scales in a Marine Stable Boundary Layer Dominated by a Low Level Jet', *Boundary-Layer Meteorol.* **76**, 211-232.

Smedman, A., M. Tjernström, and U. Högström: 1993, 'Analysis of the Turbulence Structure of a Marine Low-level Jet', *Boundary-Layer Meteorol.* **66**, 105-126.

Sun, J., D. Vandemark, L. Mahrt, D. Vickers, T. Crawford, and C. Vogel: 2001, 'Momentum Transfer over the Coastal Zone', *J. Geophys. Res.* **106**, 12,437-12,488.

Vickers, D. and L. Mahrt: 1997, 'Quality control and flux sampling problems for tower and aircraft data', *J. Atm. and Oc. Tech.* **14**, 512-526.

Vickers, D., L. Mahrt, J. Sun, and T. Crawford: 2001, 'Structure of Offshore Flow', *Mon. Wea. Rev.* **129**, 1251-1258.

Winstead, N.S. and P.D. Mourad: 2000, 'Shallow Great Lake-Scale Atmospheric Thermal Circulation Imaged by Synthetic Aperture Radar', *Mon. Wea. Rev* **128**, 3654-3663.

Winstead, N.S., T.D. Sikora, D.R. Thompson, and P.D. Mourad: 2002, 'Gravity Waves Can Directly Influence Surface-layer Stress During a Cold Air Outbreak, as shown by Synthetic Aperture Radar', *Mon. Wea. Rev.*, submitted 2001.

Winstead, N.S. and G.S. Young: 2000, 'An analysis of exit flow drainage jets over the Chesapeake Bay', *J. Appl. Meteorol.* **39**, 1269-1281.

Yamada, T.: 1983, 'Simulation of nocturnal drainage flows by a $q^2 - l$ turbulence closure model', *J. Atmos. Sci.* **40**, 91-106.

Young, G.S., T.D. Sikora, and N.S. Winstead: 2000, 'Inferring Marine Atmospheric Boundary Layer Properties from Spectral Characteristics of Satellite-Borne SAR Imagery', *Mon. Wea. Rev.* **128**, 1506-1520.